LBL-34918
UC-401

Lawrence Berkeley Laboratory

UNIVERSITY OF CALIFORNIA

CHEMICAL SCIENCES DIVISION

Infrared Diode Laser Studies of the Products from the Reaction $CH_2(\tilde{X}^3B_1) + O_2$ and from the Near-UV Photolysis of CH_3NCS

R.A. Alvarez
(Ph.D. Thesis)

November 1993

LOAN COPY
Circulates
for 4 weeks
Bldg. 50 Library.
LBL-34918
Copy 2

Prepared for the U.S. Department of Energy under Contract Number DE-AC03-76SF00098

DISCLAIMER

This document was prepared as an account of work sponsored by the United States Government. Neither the United States Government nor any agency thereof, nor The Regents of the University of California, nor any of their employees, makes any warranty, express or implied, or assumes any legal liability or responsibility for the accuracy, completeness, or usefulness of any information, apparatus, product, or process disclosed, or represents that its use would not infringe privately owned rights. Reference herein to any specific commercial product, process, or service by its trade name, trademark, manufacturer, or otherwise, does not necessarily constitute or imply its endorsement, recommendation, or favoring by the United States Government or any agency thereof, or The Regents of the University of California. The views and opinions of authors expressed herein do not necessarily state or reflect those of the United States Government or any agency thereof or The Regents of the University of California and shall not be used for advertising or product endorsement purposes.

Lawrence Berkeley Laboratory is an equal opportunity employer.

DISCLAIMER

This document was prepared as an account of work sponsored by the United States Government. While this document is believed to contain correct information, neither the United States Government nor any agency thereof, nor the Regents of the University of California, nor any of their employees, makes any warranty, express or implied, or assumes any legal responsibility for the accuracy, completeness, or usefulness of any information, apparatus, product, or process disclosed, or represents that its use would not infringe privately owned rights. Reference herein to any specific commercial product, process, or service by its trade name, trademark, manufacturer, or otherwise, does not necessarily constitute or imply its endorsement, recommendation, or favoring by the United States Government or any agency thereof, or the Regents of the University of California. The views and opinions of authors expressed herein do not necessarily state or reflect those of the United States Government or any agency thereof or the Regents of the University of California.

LBL-34918
UC-401

Infrared Diode Laser Studies of the Products from the Reaction $CH_2(\tilde{X}\ ^3B_1) + O_2$ and from the Near-UV Photolysis of CH_3NCS

Ramón Arturo Alvarez
Ph.D. Thesis

Department of Chemistry
University of California

and

Chemical Sciences Division
Lawrence Berkeley Laboratory
University of California
Berkeley, CA 94720

December 1993

This work was supported by the Director, Office of Energy Research, Office of Basic Energy Sciences, Chemical Sciences Division of the U. S. Department of Energy under Contract No. DE-AC03-76SF00098.

recycled paper

Abstract

Infrared Diode Laser Studies of the Products from the Reaction CH_2 ($\tilde{X}$ $^3B_1$) + O_2 and from the near-UV Photolysis of CH_3NCS

by

Ramón Arturo Alvarez

Doctor of Philosophy in Chemistry

University of California at Berkeley

Professor C. Bradley Moore, Chair

The absolute yields of the stable carbon containing products CO, CO_2, and H_2CO formed in the reaction of triplet methylene ($\tilde{X}$ $^3B_1 \equiv CH_2$) with O_2 have been determined using a flash kinetic spectrometer. CH_2 radicals were generated by excimer laser photolysis of ketene and product formation was monitored by time-resolved infrared diode laser absorption. The reaction was carried out in a static gas cell at room temperature (T = 298 ± 3 K) with total pressures in the range 1 - 25 torr. The measured product yields were CO, 0.34 ± 0.06; CO_2, $0.40^{+0.09}_{-0.07}$; and H_2CO, 0.16 ± 0.04. The rate constants for production of CO and CO_2 were equivalent to the published rate constant for removal of CH_2. Additionally, indirect evidence indicated that the yield of OH is 0.30 ± 0.05.

The ultraviolet spectrum of methyl isothiocyanate ($CH_3NCS \equiv$ MITC) and the quantum yield for its dissociation into methyl isocyanide (CH_3NC) and atomic sulfur at 308 nm, $\Phi = 0.98 \pm 0.24$, were measured. MITC is widely used as a fumigant and readily enters the atmosphere during and after application. The results indicate that photodissociation

by sunlight is an effective pathway for the removal of MITC from the atmosphere. A mechanism is proposed to account for the observed formation of methyl isocyanate (CH_3NCO) as a secondary product in controlled laboratory studies.

E. Bradley Moore

Table of Contents

Chapter 1. Absolute Yields for Production of CO, CO_2, and H_2CO from the Reaction CH_2 ($\tilde{X}$ $^3B_1$) + O_2

I. Introduction 1

II. Experimental 6

II.A. Infrared Diode Laser Spectrometer 6

II.B. Photolysis Laser 8

II.C. Optical Alignment and Detection 9

II.D. Triggering Scheme 11

II.E. Flash Kinetic Data Acquisition 12

II.F. Spectroscopic Data Acquisition 14

II.G. Data Reduction 15

II.H. Sample Handling and Analysis 17

II.I. Temperature 18

III. Kinetic Scheme and Results 18

III.A. Radical Generation 18

III.B. Product Formation 21

III.B.1. CO Branching Ratio 22

III.B.2. CO Production Rate and Vibrational Distribution 23

III.B.3. CO_2 Branching Ratio and Production Rate 30

III.B.4. H_2CO Branching Ratio 31

III.B.5. OH Branching Ratio 33

IV. Discussion 33

IV.A. Comparison to Other Studies 33

IV.B. Reaction Mechanism 36

V. Conclusion 38

VI. References 39

Tables 42

Figures 45

Chapter 2. Quantum yield for production of CH_3NC in the photolysis of CH_3NCS

I. Introduction 63

II. Experimental 65

III. Results and Discussion 67

III.A. Ultraviolet Absorption Spectrum of MITC 67

III.B. Fundamental Photochemistry of MITC 68

III.C. Secondary (Photo)chemistry and Environmental Consequences 72

IV. Conclusion 76

V. References 77

Tables 79

Figures 82

Appendix 1. Definition of Beer's Law 90

List of Tables

1.1. *Ab initio* values for relative energies of CH_2O_2 isomers and barriers to their interconversion and decomposition. 42

1.2. Summary of CO yield measurements. 43

1.3. Summary of CO_2 yield data. 44

2.1. Calculated photolysis rate of MITC. 79

2.2. Summary of FTIR analysis of CH_3NC production. 80

2.3. Summary of prompt CH_3NC production measurements. 81

List of Figures

1.1. Calculated ΔH_{rxn} for possible products and intermediates. 45

1.2. Schematic of infrared diode laser flash kinetic spectrometer. 46

1.3. Schematic of trigger circuit for flash kinetic data acquisition. 47

1.4. Schematic of delay generator circuit. 48

1.5. Flowchart of the spectral acquisition program FLASH. 49

1.6. Flowhart of the interrupt subroutine in FLASH. 50

1.7. Flowchart of the graphics subroutine in FLASH. 51

1.8. Schematic of interface circuit and hardware connections required for spectral acquisition using FLASH. 52

1.9. Sample CO spectrum acquired using FLASH. 53

1.10. Stern-Volmer plot of loss of CO photolysis product due to ketene collisional self-quenching. 54

1.11. Normalized CO(v=1-4) rise profiles. 55

1.12. Typical $^{12}CO(v=0)$ rise profiles and fits to eq 15. 56

1.13. Plot of measured CO(v=1) decay rates *vs.* $[CH_2{}^{13}CO]$. 57

1.14. Plot of observed CO production rates, $k_1[O_2]$, *vs.* $[O_2]$. 58

1.15. Sample $^{13}CO_2$ rise profile and fit. 59

1.16. Plot of measured $^{13}CO_2$ production rates *vs.* $[O_2]$. 60

1.17. Plot of H_2CO yield *vs.* relative scavenger to ketene pressure. 61

1.18. Sample ^{13}CO rise exhibiting a secondary contribution from the reaction OH + $CH_2{}^{13}CO$. 62

2.1. Possible fates of a pesticide in the environment. 82

2.2. Ultraviolet spectrum of CH_3NCS. 83

2.3. Beer's Law plot of MITC absorbance at 308 nm. 84

2.4. FTIR spectrum of products resulting from the 308-nm photolysis of 0.67 torr MITC in 740 torr N_2. 85

2.5. CH_3NC temporal profiles from MITC photolysis. 86

2.6. Rate constant for secondary production of CH_3NC. 87

2.7. Attenuation of CH_3NC signal due to added S-atom scavenger. 88

2.8. FTIR spectrum of products resulting from the 308-nm photolysis of 0.49 torr MITC, 62 torr O_2, and 250 torr Ar. 89

Acknowledgements

This dissertation could not have been completed without the help and support of a number of people. I would now like to express my gratitude and acknowledge their contributions.

The guidance and encouragement provided by Professor C. Bradley Moore was inspiring. My development as a scientist benefitted from our frequent interaction and owes much to Brad's attention to detail and to his healthy skepticism. The Moore group was fortunate to have had Ned Lovejoy and Miguel Rodriguez in its ranks, if only for a short time. Their selfless assistance was invaluable to the eventual success of these experiments. I learned much about the design and analysis of kinetics measurements from Ned. Miguel built and maintained the majority of the electronic accessories employed in the actual data acquisition. I-Chia Chen, Dave Darwin, John Harrison, Jeff Petty, Charles Pibel, and Horst Clauberg also provided technical assistance at crucial times.

A collective and heartfelt thank-you goes out to the thirty-or-so Moorons who breathed life into the halls of the D-level during my stay here. They were good friends both in and out of the lab. Ned got me to navigate the gnarliest mountain bike trails in the East Bay, Michael and Jeff were great running partners, and Penny led me on my first run up the fire trail. Miguel and Inma enhanced my Spanish vocabulary and promised future lodging. Charles, Miguel, and Roger provided many culinary inspirations, and while the same can't be said of Harry, he did ably demonstrate how to stretch one's food dollar. Charles, Art, and Jason could always be counted on for insight about many things best-described as outside the mainstream. Rich, Ashfaq, and Michael were

congenial lab-mates, always willing to engage in some banter while my cell (slowly) pumped out. Jeff often looked after my traps as if they were his own. Sang Kyu, my kindhearted classmate, donated the paper on which this is written. Jackie Denney organized numerous memorable picnics and resolved many administrative snafus. The group softball team faded past the league cellar and out of existence, but the players always held their heads high. Although not a Mooron, Steve Muskal deserves special credit for his part in a number of adventures and for his consistently high standards, whether they regard science, frisbee, chess, bowling, or barbeque supplies.

I would like to acknowledge the moral, spiritual, and financial support that my family has provided throughout my educational career. My mother and father, Nani and Jose, have always expressed their full confidence in all my decisions, and especially in the eventual completion of this work. I would also like to thank the Hillman family, who became my surrogate family on the West coast, for their encouragement and support.

Susan Hillman has witnessed virtually the entire course of my graduate career: the good times and, more often, the tough times. Her friendship, love, and patience were constant throughout. Susan has been such an important part of my life that it would be impossible to fully acknowledge all her contributions. I can only pledge to be as supportive and understanding during her graduate career.

Chapter 1. Absolute Yields for Production of CO, CO_2, and H_2CO from the Reaction CH_2 ($\tilde{X}$ $^3B_1$) + O_2

I. Introduction

The understanding and accurate modeling of combustion and atmospheric chemistry systems require a complete and accurate set of elementary reactions and rate constants. The ability to define an elementary reaction step requires the measurement of both a rate constant *and* branching ratios. While the rate constants used in most models are often well established, the product branching ratios--to which a model may be more sensitive--are often not. Thus, the identification of the products formed in reactions whose rate constants are well-known is a critical area of research. The infrared tunable diode laser (TDL), covering the spectral region 3-30 μm, is well-suited for such studies since most molecules and radicals have signature absorptions in that range. Coupled with a pulsed excimer laser which generates high densities of radicals at a well-defined point in time, the TDL allows one to monitor the temporal evolution of a large number of chemical species of interest in combustion and in the atmosphere.

Triplet methylene ($^3CH_2$) is a radical formed in such chemical processes as the combustion of acetylene whose detailed chemistry remains largely uncharacterized. Direct measurements of the rate constants for reactions of $^3CH_2$ with such common species as O_2, NO, and C_2H_2 have been made within the past 20 years.[1-6] A large obstacle to that achievement was the inability to distinguish the identity and chemistry of the ground state triplet methylene from the

low-lying electronically excited singlet methylene. The rate constant, k_1, of reaction 1

$$^3CH_2 + O_2 \rightarrow \text{products} \qquad (1)$$

has been measured to be $(3.2 \pm 0.3) \times 10^{-12}$ cm^3 $molecule^{-1}$ s^{-1}.[2-4] A slight temperature dependence of the rate constant was measured over the ranges 233-433 K[4] and 295-600 K,[5] suggesting the presence of a small (1.0 - 1.5 kcal mol^{-1}) barrier to formation of the initial CH_2O_2 adduct or to its subsequent isomerization or fragmentation. At higher temperatures (1000 - 1800 K) a negative temperature dependence has been observed.[6] As indicated in Figure 1.1, there are a number of thermodynamically available product channels,[7-11] many of which have been reported in previous studies (*vide infra*). However, little conclusive, quantitative product data exists for the electronically state-specific reaction. The rate constant for the loss of singlet methylene in collisions with O_2, 7.4×10^{-11} cm^3 $molecule^{-1}$ s^{-1}, has been reported[12] and is thought to represent a combination of both collision-induced intersystem crossing and chemical reaction. The observation of the same overall products from $^1CH_2 + O_2$ as from reaction 1 suggests the possibility that $^1CH_2$ is first collisionally converted to $^3CH_2$, which then reacts according to reaction 1.[13] Alternatively, the reaction may proceed directly upon the same potential energy surface with modest differences resulting from the added ~3150 cm^{-1} of energy in $^1CH_2$.

The transformation from reactants to products in reaction 1 is governed by the topography of the multidimensional CH_2O_2 potential

energy hypersurfaces. The species and dynamics involved in a chemical transformation can in principle be inferred from a detailed study of the different product channels accessed, their branching ratios, and the energy disposal into the individual products. The reaction between two triplet species can proceed via singlet, triplet, or quintet surfaces. Four distinct isomeric species exist as potential minima on the CH_2O_2 hypersurfaces: peroxymethylene (**I**), dioxirane (**II**), methylenebis(oxy) (**III**), and formic acid (**IV**).

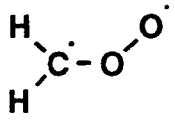

I

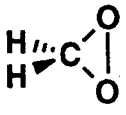

II

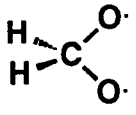

III

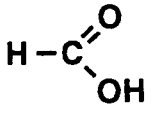

IV

Ab initio calculations to determine the energies and geometries of the low-lying electronic states of species **I** - **III** (Figure 1.1) have been reviewed.[7] Additionally, potential energy barriers to some of the interconversions between species **I** - **IV** and barriers to their decomposition have been calculated. Table 1.1 summarizes the available theoretical data on the CH_2O_2 system.[7,8,14-23]

The intermediate CH_2O_2 species (**I** - **IV**) and their excited electronic states have also been hypothesized to occur in the ozonolysis of ethylene[24-28] and in the photolytic decomposition of formic acid.[29-32] The ozonolysis of ethylene is thought to proceed through the formation of molozonide **V**

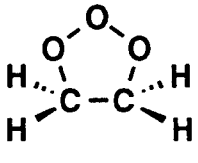

V

and subsequent decomposition to give formaldehyde and the Criegee intermediate, **I**.[24] The reaction is believed to be important in urban atmospheres and over tropical forest areas;[25] and as a night-time process which generates radicals, it could contribute to "neuartige Waldschäden" (new type forest decline) in Central Europe.[33]

The first reports of stable products arising from the reaction of CH_2 (electronic state unspecified) with O_2 mentioned CO, CO_2, H_2CO, and HCOOH.[34,35] Using radioisotopically labelled ketene, Rowland and coworkers concluded that triplet methylene was quantitatively oxidized by O_2 to yield equal amounts of CO and CO_2, and that H_2 was eliminated intramolecularly from a CH_2O_2 adduct.[13,36] They also reported indirect evidence for the formation of translationally hot H atoms.[13] Eberius *et al.* modeled the observed production of CO_2 in the early part of lean C_2H_2/O_2 flames as due to the attack of CH_2 (state unspecified) on O_2.[37] CO laser absorption by vibrationally excited CO(v ≤ 13) in the flash photolysis of low pressure $CH_2X_2/O_2/SF_6$ mixtures (X = Br, I) has been measured.[38,39] The observed vibrational distribution is rationalized as resulting from the formation of CO by a radical and a molecular channel, reactions 1a and 1b, respectively (electronic state unspecified).

$$CH_2 + O_2 \rightarrow HCO + OH \qquad (1a)$$

$$CH_2 + O_2 \rightarrow CO(v) + H_2O \qquad (1b)$$

The HCO was said to rapidly dissociate unimolecularly to give H + CO(v). The model indicated that the radical channel accounts for 70% of the CO product and the molecular channel for 30%. Vinckier and

Debruyn used mass spectrometric sampling of a $C_2H_2/O/O_2$ fast flow reactor system to monitor the direct production of HCO, attributed to reaction 1.[5,40] However, no formic acid was detected in their experiment.[5] Lee and Pimentel studied the chemiluminescence from a photolyzed $CH_2N_2/O_2/Ar$ matrix as it was slowly warmed and detected vibronic progressions which indicated that for some molecules nearly all the available exothermicity from reaction 1 (63,000 cm^{-1}) is converted into electronic excitation of the (unquantified) product HCOOH (A' $^1A'$).[41] Hatakeyama *et al.* detected CO, CO_2, H_2CO, HCOOH, and O_3 as products of the broadband irradiation ($310 < \lambda < 400$ nm) of dilute ketene mixtures in an atmosphere of air.[42] Ozone is believed to be formed by the reaction of molecular oxygen with O atoms produced in the oxidation of triplet methylene:

$$^3CH_2 + O_2 \rightarrow H_2CO + O(^3P) \qquad (1c).$$

Additionally, they reported evidence for reactions of a stabilized peroxymethylene (**I**) intermediate. Böhland *et al.* monitored the progress of reaction 1 by LMR of an isothermal discharge flow system and observed the OH and HO_2 radicals.[3] HO_2 was postulated to arise from the secondary reaction of HCO with O_2, but an HCO signal could not be obtained on their instrument. They assign an upper limit of 0.1 to the yield of reaction 1c. Horie and Moortgat recently attempted to reproduce the results of Hatakeyama *et al.* and detected essentially the same products.[43] However, there was no evidence that indicated the formation of a stabilized CH_2O_2 intermediate in their experiment.

Bley *et al.* placed upper limits on the H atom and OH radical producing channels of 0.2 and 0.3, respectively.[4] Reaction 1 occurring in a shock wave (1000 < T < 1800 K) was reported to lead to a $CO:CO_2$ product ratio of 4:1, H and O atom yields of 20% and 10%, respectively, and an OH yield of <5%.[6] Finally, Knyazev *et al.* have reported the H atom yield from reaction 1 as occurring in a $O/CH_2CO/O_2$ system to lie between 1.00 and 1.75.[44]

II. Experimental

Darwin has described the salient features of the experimental apparatus.[2,45] In addition to the work described in this thesis, the apparatus was also used to study the yield of CO in the reaction $^1CH_2$ + CH_2CO[46] and the intramolecular carbon atom exchange in ketene.[47] In this experiment, laser flash photolysis of ketene at 351 nm in a room temperature static gas cell generates uniquely $^3CH_2$ radicals.[48] A CW diode laser resonant with a rovibrational transition of a product molecule probes time-resolved changes in absorbance due to changes in concentration. Changes performed on the system since 1988 along with brief descriptions of the individual components and the data acquisition scheme are now presented. A schematic of the apparatus is shown in Figure 1.2.

II.A. Infrared Diode Laser Spectrometer

The formation of products was monitored with a diode laser spectrometer. Laser diodes which emit infrared light are made from lead chalcogenides (PbSSe, PbSnSe, PbSnTe), where the specific salt and stoichiometry determine the emission range.[49] The output

frequency of a laser diode depends on its temperature (which also controls the size of the resonant laser cavity defined by the front and rear surfaces of the diode crystal), and this serves as the source of its tunability. Typical diodes span a total tuning range of 150 - 200 cm^{-1}, with a resolution of ~0.0003 cm^{-1}. Mode breaks prevent continuous tuning over the entire range, and most diodes provide tunable light over ~1 cm^{-1} intervals with gaps of ~1 cm^{-1} in between. Frequency fine-tuning is afforded by the heating effect of the injection current.

A critical parameter in successfully measuring transient product yields is the frequency stability of the diode laser output. Both fast frequency jitter (μs timescale) and slow frequency drift (seconds to minutes timescale) degrade the measured S/N ratios. The fast frequency jitter is controlled by the current stability of the laser driver (LCM), which is specified at 50 μA peak-to-peak, and the tuning rate of a specific diode. For a diode with a tuning rate of 1500 MHz mA^{-1} (the value for the Moore group's Spectra Physics 2100 cm^{-1} diode) this corresponds to a frequency jitter of 75 MHz. The Doppler width of a CO line at 2100 cm^{-1} is ~150 MHz, so that the maximum S/N which could be achieved is ~2 per shot, disregarding other sources of noise. In this estimate, the signal is the magnitude of a transient absorption obtained while sitting on the peak of a CO line and the noise is the peak-to-peak fluctuation of the signal level due to excursions from line center. Selection of laser diodes with low tuning rates is a prerequisite for optimal S/N. The Moore group's 2100 cm^{-1} Mütek diode possesses a tuning rate of 600-800 MHz mA^{-1} and leads to the expected improvement in S/N over the Spectra Physics diode. It should be mentioned that the age of a diode also tends to exacerbate

the frequency jitter. Laser Photonics has developed an all-digital laser current controller (L5830) with stated current noise amplitudes of 5 μA rms which could also enhance the present experimental sensitivity.

Drift of the laser frequency on longer timescales (seconds to minutes) is due mainly to temperature drift. Probing off the peak of an absorption feature reduces the magnitude of a measured transient absorption, effectively reducing the S/N as well as providing a source of systematic error in these experiments. The systematic error arising from slow drift of the laser frequency off the absorption maximum was minimized (< 5%) by employing short averaging times (maximum 160 shots at 3.33 Hz). Experiments were attempted using a frequency stabilization scheme, as described by Darwin,[45] by locking onto the peak of a reference line. The stabilization did not afford significantly better S/N than that obtained under free-running conditions and was therefore abandoned.

Another factor which can degrade system performance is optical feedback. The placement of normal incidence windows, irises, or filters in the IR beam path can result in the formation of an external laser cavity which creates uncontrolled optical feedback.[50] In these experiments, this effect was observed as enhanced frequency jitter or amplitude instability. Because the feedback depends on the precise optical alignment, minor adjustments are usually sufficient to remove this noise source.

II.B. Photolysis Laser

An excimer laser (Lambda Physik EMG 201 MSC) running on XeF and operating with unstable resonator optics was used to photolyze

ketene. Typical pulse energies used were 20-60 mJ cm^{-2}. With a fresh fill of XeF, the excimer output was ~100 mJ $pulse^{-1}$ at 23 kV. Addition of some Ne in place of He buffer (400 mbar) gave higher pulse energies: 140 mJ $pulse^{-1}$ at 23 kV. The excimer was triggered with a fiber optic cable to reduce ground loops. This excimer performed consistently well, with the exception of the integrity of its seals. Locating and fixing leaks was a frequent endeavor. The preionization pins in particular became a progressively chronic source of leaks in the laser cavity. The problem escalated to the point that by October 1990 at least 34 out of the 84 pins were concurrently leaking. The pin design was inherently flawed: the ceramic pins could not handle the stress combination of high voltages and corrosive gas mixtures. The manufacturer developed new, slightly thicker pins coated with teflon to correct the problem. However, the new pins could not be retrofitted into the old cathode plate assembly, so an entirely new plate with preionization pins was installed (the electrode was not replaced). The new pins have proved worthy and have sprung no leaks over nearly a 2-year period. In the process of replacing the cathode plate, the PVDF (polyvinilydenefluoride) channel between the two electrodes devoloped a crack near the rear window adapter and also had to be replaced. At the time of writing the leak rate was < 100 mbar per month, a negligible effect.

II.C. Optical Alignment and Detection

A 1" CaF_2 f/1 lens (Infrared Optical Products) mounted on an x-y-z translation stage was used to collimate the divergent diode laser beam. The UV and IR were coupled with a 45° dichroic reflector

(Acton Research) and propagated concentrically down the length of a 78.3 cm pyrex reactor sealed with CaF_2 windows and decoupled with another dichroic mirror. The cylindrical reactor has a 16 cm diameter; the large volume prevents significant precursor depletion or product buildup. The beam diameters inside the reactor were typically 3-6 mm and 5-7 mm for the IR and UV beams, respectively; in all cases the IR beam was smaller than the UV beam. Irises were used to select the desired beam diameters. In some experiments a 1 m spherical Al mirror was placed before the dichroic coupler to ensure good overlap and gain IR throughput (the collimated IR beam diameter was sometimes as large as 7-8 mm). The IR beam would thus come to a soft focus (2 - 3 mm) about 3/4 of the way through the cell. A 0.75 m monochromator (Spex Industries) was used to select a single mode of the diode laser output. The grating was blazed at 16 μm and was operated in third order for most experiments (fourth order for some CO_2 experiments).

The UV fluence was measured with a volume absorbing disc calorimeter (Scientech 38-0105) calibrated by electrical substitution. A mask with a 5.6 mm hole was placed between the exit window of the cell and the dichroic decoupler to allow only the portion of the UV beam being probed by the IR laser onto the power meter. The changes in the IR signal levels were monitored by an InSb photovoltaic detector (Cincinatti Electronics, 2.0 or 0.25 mm diameter element) or a HgCdTe photoconductive detector (SBRC $1 mm^2$ element) whose outputs were fed into a transient digitizer (Tektronix 7912AD). The digitizer amplifier and time base were factory calibrated, and the time base calibration was periodically checked against a 1 MHz quartz oscillator.

II.D. Triggering Scheme[51]

The cold head of the helium refrigerator (CTI Cryogenics, Model 22C) which cools the laser diodes employs a direct-drive, constant speed motor which operates at 200 rpm on the 60 Hz power line. The duration of one piston cycle is thus 300 ms. The mechanical cycle inside the cold head introduces two problems: temperature oscillations and impact shocks delivered to the diode during the expansion and contraction phases of the piston cycle. Both produce jitter in the laser output frequency. Analysis of the vibrations by means of a microphone or a vibration meter coupled to the cold head revealed that the peak of the mechanical noise or of the vibration occurred every 300 ms, lasting ~200 ms. The remaining 100 ms is relatively quiet and serves as the window during which kinetic data is acquired, at a repetition rate of 3.33 Hz. A trigger circuit was constructed to synchronize the transient data acquisition to the cold head piston cycle and is described in detail elsewhere.[51] A schematic of the circuit is shown in Figure 1.3. Use of this circuit also minimizes the effect of amplitude fluctuations in the diode laser signal observed at the detector. This is due to the fact that the impact shocks from the piston cycle are strong enough to cause the entire optical table and mounted optical hardware to vibrate in a complex but periodic fashion.

The output from the trigger circuit is sent to a delay generator which allows for a variable delay to be set between the digitizer and the excimer triggers. This delay is necessary so that the baseline value of the IR signal can be recorded prior to the excimer laser pulse (the experimental observable is ΔI). A schematic of the circuit which controls the delay is presented in Figure 1.4. This circuit can also be

triggered internally if the cold head trigger unit is not used. There is also an output for triggering an external shutter which blocks the excimer beam and which allows alternate shots to be subtracted, in contrast to adding N shots and subsequently subtracting N shots with the UV beam blocked, as is done in these experiments. Finally a second input to the delay box serves to trigger only the digitizer. This permits a second trace to be read into the Channel B input of the digitizer. This option was developed in order to normalize for pulse-to-pulse energy fluctuations in the UV beam (typically ±10%), but it was never found necessary to implement. Because all experiments involved averaging the signals resulting from 32 - 160 excimer shots, the measured *average* pulse energy was an adequate indicator of the laser energy in a particular experiment.

II.E. Flash Kinetic Data Acquisition

A transient signal was acquired by setting the laser frequency at the peak of a desired rovibrational transition, summing the digitized detector response to the change in diode laser intensity during the period just before and up to 200 μs after each of 32-160 excimer laser pulses entered the reactor, and subtracting an equal number of pulses with the UV beam blocked to remove any instrument response and pickup. Occasionally, as in the H_2CO experiments, it was necessary to perform the subtraction with the UV beam entering the cell and the diode laser frequency set off resonance in order to remove spurious transients due to broadband absorbances not related to the probed species. A reference cell containing the probed species is used to locate the laser frequency of a desired absorption line. A 1.5 m pyrex

cell has been built to vibrationally excite a reference sample in a DC discharge, in order to locate the frequency of transient absorbers. For example, transitions from CO($v \leq 5$) are detected by flowing 0.3 torr CO in 1.0 torr N_2 through a 3 mA discharge nominally at 5-10 kV. A diode laser (Mütek MDS 2020) covering the frequency range 2050 - 2200 cm^{-1} monitored CO, with typical single mode power >1 mW along with exceptional mode quality and low tuning rate. Lower performance diodes (Spectra Physics SP5615) lasing in the regions 2260 - 2360 and 1685 - 1820 cm^{-1} were used to probe $^{13}CO_2$ and H_2CO, respectively. The transitions used for detection were: R(11), R(9), R(7), and R(5) of ^{12}CO;[52] R(20) of ^{13}CO;[52] R(8), R(28), and R(40) in the ν_3 band of $^{13}CO_2$;[52] and ($13_{1,13} \leftarrow 12_{1,12}$) in the ν_2 band of H_2CO.[53]

Determination of an absolute product yield requires the measurement of *both* the transient product density and a reference signal which can be converted to give the initial CH_2 density. CO from ketene photolysis was thus used as an internal actinometer. The CO yield determinations can be performed with the same diode on the same day, by taking successive traces on nearby ^{12}CO and ^{13}CO lines (using the same gas fill, if so desired). To measure the transient absorbances of other products, whose rovibrational frequencies are significantly different, another diode must be used and so the optical path must be realigned. In this case, the CO from the photolysis of a normal ketene sample under similar conditions (i.e., identical precursor and buffer gas pressures with Ar replacing O_2), corrected for collisional broadening, serves as the standard to which the measured CO_2 and H_2CO product concentrations are ratioed.

II.F. Spectroscopic Data Acquisition

To convert a measured transient absorption into concentration, linestrengths or peak absorption coefficients had to be measured. A new spectral acquisition scheme, operating on an IBM PC AT, was thus set up. The program FLASH scans the diode laser current and can simultaneouly read in 1 - 3 channels of data at each frequency step. The 3 channels are a transient spectrum, a reference gas spectrum for absolute frequency calibration, and an etalon fringe pattern to determine relative frequency spacings. The acquisition of a complete 3-channel spectrum requires splitting the mode-selected diode laser beam into 3 components, 3 infrared detectors, 2 lock-in amplifiers, and a boxcar integrator. The lack of 3 detectors prevented us from acquiring an actual 3-channel spectrum, but the routine was used successfully to collect stable reference spectra for calibration purposes. A brief functional description of the software and hardware follows.

Flowcharts of the program FLASH and the subroutines which control the interrupt and interactive graphics are displayed in Figures 1.5, 1.6, and 1.7, respectively. The diode laser frequency is tuned by applying a voltage ramp from a computer controlled D/A circuit (Computer Boards, Inc., 12 bits with external reference set to 4.095 V) to the diode laser current controller. For a laser with a tuning rate of 0.02 cm^{-1} mA^{-1}, an effective step size of 4×10^{-4} cm^{-1} could be achieved. Reference and etalon spectra were obtained by demodulating the mechanically chopped IR signal (100 Hz) at each frequency step with a lock-in amplifier (PAR, Model 124) whose output was read into the PC through a 12 bit A/D converter (Computer Boards, Inc.) and stored. To collect transient spectra, the output from a boxcar

integrator (PAR 162) is similarly read into the PC. The data is read into the computer on the basis of interrupts (level 5 is used).

Figure 1.8 is a schematic of the hardware connections which are needed to run the program FLASH. The excimer laser is fired from the computer (counter 0 output) via a fiber optic cable. A photodiode triggered by some scattered light from the excimer beam then triggers the boxcar integrator and the counter 1 gate. After a programmed 2 ms delay (set in subroutine init_AD_DA) which allows the boxcar to finish processing the transient data, the counter 1 output triggers the interrupt to begin reading the values from the 3 channels of the A/D converter. Counter 2 is used as a clock (50 kHz) which serves as a reference for the counter 0 and 1 clocks. Counter 0 is used as a rate generator; it pulses at a fixed frequency (the repetition rate) set in the main program menu and triggers the excimer. If the counter 0 gate goes low (0 V) then the counter 0 output will stop pulsing. This permits other tasks to be performed without firing the excimer. In the special case where only a reference spectrum is desired, a BNC output from the back of the interface box provides an electrical pulse synchronous with the excimer trigger (counter 0 output). This pulse can be fed directly into the interrupt which then sends the program to read in the reference signal input. A representative scan of a CO vibration-rotation line, acquired with the FLASH routine, is displayed in Figure 1.9.

II.G. Data Reduction

To calculate the reaction yield of a product, it is necessary to derive number densities from the experimental observables. The

experiment measures the transient change, ΔI, in the CW diode laser signal, I_0, due to absorption by species produced by reaction of CH_2. Product concentrations were calculated using Beer's Law (see Appendix 1). The absorption coefficient at line center α can be either directly measured by experiment or calculated from published linestrength data by the relation $\alpha = S\phi(\nu_0)$, where S is the linestrength or integrated line intensity and $\phi(\nu_0)$ is the lineshape function at line center, ν_0. For molecules not in a collision-free environment, the lineshape is described by a Voigt profile, a convolution of a Doppler-broadened Gaussian profile and a collision-broadened Lorentzian profile. The lineshape function at line center for a collisionally broadened line is given by

$$\phi(\nu_0) = \frac{2}{\Delta\nu_D}\left(\frac{\ln 2}{\pi}\right)^{1/2} V(a)$$

where $\Delta\nu_D$ is the Doppler width and V(a) is the Voigt function parametrized by the Voigt parameter a, which is a measure of the relative importance of collision and Doppler broadening. V(a) approaches unity as the total pressure approaches zero. V(a) is determined empirically in these experiments by measuring the peak absorbance of a sample of CO, CO_2, or H_2CO as a function of added collision partners. Published linestrength values were used to determine the CO densities[54] and the peak absorption coefficients were directly measured in order to determine other product densities.

Peak absorption coefficients were measured by scanning the diode laser frequency across an absorption line at different sample pressures using the program FLASH. The baseline at the absorption

maximum was obtained by interpolating a smooth functional fit to the baseline beyond both wings of the absorption line. The peak of the absorption line was taken to be the point of maximum absorbance; accounting for the finite diode laser frequency step size, this procedure underestimates the peak absorbance by no more than 5%. Figure 1.9 illustrates typical data which was aquired to determine peak absorption coefficients and collisional broadening parameters.

II.H. Sample Handling and Analysis

Reactant and precursor pressures were measured with 10 and 100 torr absolute capacitance manometers (MKS Instruments Type 222) which were calibrated against both a mercury manometer and a 1 torr transfer standard capacitance manometer (MKS Instruments Type 390) by volume expansions. Ketene and its isotopomers were synthesized as described elsewhere.[47] A trap-to-trap distillation from 143 K to 77 K was performed to purify the ketene. Oxygen (Alphagaz Research Grade, > 99.997%), Argon (Liquid Air Corporation Industrial Grade, > 99.995%), and SF_6 (Matheson Instrument Grade, > 99.99%) were used without purification. H_2CO was obtained by cracking para-formaldehyde at 400 K and purified by trap-to-trap distillation from 184 to 77 K.[55] 2-methyl-2-butene (Aldrich, > 99+%) was degassed and purified by trap-to-trap distillation from 195 to 77 K, discarding the last 10-20%. The relative abundance of $^{13}CO_2$ in the reference CO_2 sample (Matheson Bone Dry, > 99.8%) was determined to be 0.01094 with an isotope ratio mass spectrometer (VG Instruments Prism Series II).

II.I. Temperature

The temperature for all yield, peak absorption coefficient, and rate constant measurements was 298 ± 3 K. The D80 laboratory temperature was subject to fluctuations over periods of several hours ever since the auxiliary chiller which regulated the temperature broke in 1988. The construction in 1991 of another experimental apparatus (for C-H bond activation studies) and the resultant added heat load only made matters worse, leading to a higher overall baseline temperature (each apparatus raises the room temperature 1-2 degrees when fully operational). An average temperature of 298 K was thus assumed for all experiments, and the fluctuations factored into the uncertainty in the results.

III. Kinetic Scheme and Results

III.A. Radical generation

Triplet methylene (hereafter referred to as CH_2) is generated by the 351 nm photolysis of ketene:[48]

$$CH_2CO + h\nu \rightarrow (CH_2CO)^{\dagger} \rightarrow CH_2\ (\tilde{X}\ ^3B_1) + CO.$$

The average thermal (300 K) energy[56] of 450 cm^{-1} and the energy of a 351 nm photon bring ketene just 650 cm^{-1} above the dissociation threshold. At this energy no singlet methylene is formed (< 0.5%), and the dissociative lifetime of ketene is ~11 ns.[57] The nascent CO photolysis product is rotationally hot due to the presence of a small (1330 cm^{-1}) exit barrier,[58] but this excess energy is thermalized after

a few collisions. A minor fraction (~10%) of the CH_2 is formed with one quantum of bending vibrational excitation.[48,59] Typical initial methylene concentrations employed were 10^{12} - 10^{13} molecules cm^{-3}. The CO produced from the photolysis of CH_2CO serves as an internal actinometer: the concentrations of CH_2 and CO are equal just after the laser pulse: $[CH_2]_0 = [CO]_{phot}$. This fact permits accurate conversion of measured relative transient absorbances to absolute yields. Reactions 3 - 6, discussed individually below, account for the CH_2 photolysis yield from an isotopically labelled ketene precursor.

$$CH_2{}^{13}CO + h\nu \rightarrow (CH_2{}^{13}CO)^{\dagger} \quad (3)$$

$$(CH_2{}^{13}CO)^{\dagger} \rightarrow CH_2 + {}^{13}CO \quad (4a)$$

$$(CH_2{}^{13}CO)^{\dagger} + M \rightarrow CH_2{}^{13}CO + M^* \quad (5a)$$

$$(CH_2{}^{13}CO)^{\dagger} \rightarrow ({}^{13}CH_2CO)^{\dagger} \quad (6)$$

$$({}^{13}CH_2CO)^{\dagger} \rightarrow {}^{13}CH_2 + CO \quad (4b)$$

$$({}^{13}CH_2CO)^{\dagger} + M \rightarrow {}^{13}CH_2CO + M^* \quad (5b)$$

At the pressures employed in these experiments (1 - 25 torr) a number of collisions may occur before an excited ketene molecule, $(CH_2CO)^{\dagger}$, dissociates. If these collisions remove the excess energy by V-V, V-R, or V-T processes, some of the excited ketene molecules will not dissociate (reaction 5). These quenching processes reduce the quantum yield for dissociation from its collision-free value of unity. A crude Stern-Volmer analysis applied to ketene collisional self-quenching is presented in Figure 1.10 to illustrate this point. A model in which an excited ketene molecule will either dissociate or be

collisionally quenched by a single collision predicts that the photolytic CO product density in pure ketene should vary as

$$\frac{1}{[CO]} = \frac{1}{[\text{ketene}]\phi} + \frac{k_5}{k_4\phi} \qquad (2)$$

where ϕ denotes the fraction of ketene molecules initially excited, k_5 is the bimolecular quenching rate constant, and k_4 is the unimolecular dissociation rate constant. From the intercept to slope ratio it is evident that k_5/k_4 for ketene self quenching is 0.34 $torr^{-1}$. Other reactant and bath gases similarly reduce the photolytic yield, but with varying efficiencies: relative quenching rate constants of 0.012, 0.16, and 0.19 $torr^{-1}$ were obtained for Ar, SF_6, and 2-methyl-2-butene, respectively. Some curvature in the quenching efficiency was evident in the case of 2-methyl-2-butene. In the determination of the CO_2 and H_2CO yields, errors due to collisional quenching were minimized by performing the photolysis reference and reaction signal experiments under similar conditions. For the CO yield measurement, a relatively high pressure of buffer gas is used for the photolysis experiments, and in order to obtain the reaction yield signals either a small amount of reagent O_2 is added (<15% of total pressure) or the buffer is replaced entirely by O_2, as in the case when the reference signal and reaction yield signal rely on different ketene isotopomers for precursors (see Table 1.2).

The isotopically labelled carbon atoms in the ketene precursor have been shown to undergo scrambling upon photolytic excitation (reaction 6).[47] This unimolecular process leads to the observation of ^{12}CO from the photolysis of $CH_2{}^{13}CO$. Further enhanced by isotopic

impurities (e.g. $^{12}CH_2{}^{12}CO$), the yield of ^{12}CO from the 351 nm room temperature photolysis of a typical carbonyl-labelled ketene sample can be obtained from the published ratio[47]

$$0.065 = \frac{[^{12}CO]}{[^{12}CO]+[^{13}CO]}.$$

Overall, C-atom exchange constitutes about 16% of the total measured signal of ^{12}CO, and the results are corrected to exclude this contribution.

III.B. Product Formation

In the presence of added O_2 the kinetics of triplet methylene are governed by the following reactions

$$CH_2 + O_2 \rightarrow \text{products} \qquad (1)$$

$$CH_2 + CH_2 \rightarrow C_2H_2 + 2H\ (H_2) \qquad (7)$$

$$CH_2 + CH_2CO \rightarrow \text{products} \qquad (8).$$

Reaction 8 is not an important removal process in this system ($k_8 < 2 \times 10^{-15}$ cm^3 molecule^{-1} s^{-1}).[3] The recombination rate constant of CH_2 has been measured to be faster than the gas kinetic collision rate: $k_7 = (3.1 \pm 0.8) \times 10^{-10}$ cm^3 molecule^{-1} s^{-1}.[45] With the exception of the H_2CO measurements, sufficiently high O_2 concentrations and low UV fluences were employed so that the recombination reaction does not contribute significantly to the removal of CH_2: $k_7[CH_2]_0/k_1[O_2] < 0.05$.

Multiple thermodynamically allowed branching channels exist for reaction 1:

$$CH_2 + O_2 \rightarrow (CH_2O_2)^{\dagger} \rightarrow HCO + OH \quad (1a)$$
$$\rightarrow CO + H_2O \quad (1b)$$
$$\rightarrow H_2CO + O(^3P) \quad (1c)$$
$$\rightarrow H + CO + OH \quad (1d)$$
$$\rightarrow HOCO + H \quad (1e)$$
$$\rightarrow CO_2 + 2H \quad (1f)$$
$$\rightarrow CO_2 + H_2 \quad (1g)$$
$$\rightarrow HC(O)O + H \quad (1h)$$
$$\rightarrow H_2CO + O(^1D) \quad (1i)$$
$$\rightarrow HCOOH \quad (1j).$$

The possible product channels $O(^3P, {}^1D) + H_2 + CO$, arising from the dissociation of excited H_2CO formed as a primary product, are nearly degenerate with channels 1c and 1i, but are not included in the reaction scheme. Neither channel is believed to significantly contribute to the measured yields. In this work, the yields of the stable carbon-containing products CO, CO_2, and H_2CO are determined. The primary radical products and the contribution of their secondary reactions to the observed product yields is also discussed below.

III.B.1. CO Branching Ratio

The yield of CO reaction product is the ratio of the additional CO produced in the presence of O_2 to the CO from ketene photolysis. Isotopic substitution of ^{13}C into the carbonyl or methylenic moiety of

ketene is an effective way to distinguish the photoproduct from the reaction product. For example, the $^{12}CH_2$ from the photolysis of $^{12}CH_2{}^{13}CO$ reacts with O_2 to form ^{12}CO. The absolute yield of CO from reaction 1, using $CH_2{}^{13}CO$ as a precursor and uncorrected for C-atom exchange and isotopic impurities, is given by

$$\frac{\left[{}^{12}CO\right]_{t>>\tau}}{\left[{}^{13}CO\right]_{phot}} = \frac{A\left({}^{12}CO\right)\Delta\nu_D\left({}^{12}CO\right)S\left({}^{13}CO\right)V\left(a({}^{13}CO)\right)}{A\left({}^{13}CO\right)\Delta\nu_D\left({}^{13}CO\right)S\left({}^{12}CO\right)V\left(a({}^{12}CO)\right)} \tag{9}$$

where τ represents the lifetime of CH_2, A(X) the absorbance of species X, and the rest of the terms are defined in section II.G. The Voigt function was assumed to be the same for both CO isotopes. (The use of an isotopic precursor is necessary for accurate measurements of CO but not for CO_2 and H_2CO yields. However, the nearly total absorption of the infrared probe beam by atmospheric $^{12}CO_2$ forces the use of an isotopic precursor in order to probe $^{13}CO_2$.)

Table 1.2 summarizes the results of the corrected CO yield measurements. The CO yield in reaction 1 is 0.34 ± 0.02, where the uncertainty is the 95% confidence interval for precision. Propagating the uncertainties inherent in the component terms of eq 9 (±0.04), and adding in estimates of the sources of systematic error in the experimental method (±0.02) leads to a reported branching ratio for production of CO in reaction 1 of 0.34 ± 0.06.

III.B.2. CO Production Rate and Vibrational Distribution

To show that an observed product is indeed produced directly in the title reaction, it is necessary to demonstrate the equivalence of the

measured rate constant for its production to the rate constant for removal of CH_2. The measurement of production rate constants quickly becomes cumbersome if there exists more than one channel leading to the formation of a particular species. Reaction 1d, for example, is in fact the sum of several elementary steps,

$$CH_2 + O_2 \rightarrow H + CO(v) + OH \qquad (1d_v)$$

where v represents the CO vibrational quantum number. Vibrationally excited CO($v \leq 5$) was detected as a reaction product (no attempt was made to look at higher levels). The product signals from the first 4 vibrationally excited levels of CO are shown in Figure 1.11. The main difficulty in analyzing the CO($v = 0$) rate data is deconvoluting the contributions to the signal from [CO($v > 0$)]. The experiment should be performed under conditions such that the rate of vibrational relaxation of CO($v > 0$) is much faster than the rate of reaction. The vibrational relaxation of CO(v) occurs through near-resonant v-v transfer to ketene, reaction 10.

$$CO(v) + CH_2{}^{13}CO \rightarrow CO(v - 1) + CH_2{}^{13}CO(v_2 = 1) \qquad (10)$$

To achieve the desired conditions it is necessary to use low $[O_2]$/[ketene] ratios. However, the removal of CH_2 must remain first order ($k_1[O_2] >> k_7[CH_2]_0$), so that the range of O_2 concentrations useful in the experiment is limited by kinetic restrictions. In practice, a compromise must be reached between $[O_2]$/[ketene], $[CH_2]_0$, and

S/N by photolyzing with the lowest UV fluences leading to an acceptable signal quality.

Because sufficiently low $[O_2]/[\text{ketene}]$ ratios to ensure simple first-order CO production kinetics could not be achieved, an approximate mechanism is invoked to analyze the observed CO production rate measurements:

$$CH_2 + O_2 \rightarrow CO(v = 0) + \text{products} \quad (11)$$

$$CH_2 + O_2 \rightarrow CO(v \geq 1) + \text{products} \quad (12)$$

$$CH_2 + O_2 \rightarrow \text{other products not CO} \quad (13)$$

$$CO(v \geq 1) + CH_2{}^{13}CO \rightarrow CO(v = 0) + CH_2{}^{13}CO(v_2 \geq 1) \quad (14).$$

A more detailed and complete analysis would have explicitly included the contributions from $[CO(v \geq 2)]$. Quantifying the nascent CO product vibrational energy distribution proved difficult due to rapid vibrational energy relaxation. Some general features of the distribution could nonetheless be surmised. The ratio $N_v/N_{v=0}$ falls monotonically with v, more rapidly than reported by Lin and coworkers.[38,39] By extrapolating the decays of the observed CO(v = 2) and CO(v = 3) signals to time = 0, it could be estimated that direct production of CO(v = 2) accounts for 2 - 3% of the initial methylene formed and CO(v = 3) for 0.4 - 1.0%. Since the production of CO molecules with 2 or more quanta of vibrational excitation thus represents only ~10% of the total CO signal and ~25% of the vibrationally excited CO (*vide infra*), the approximate mechanism consisting of reactions 11-14 should provide values of k_1 accurate to within experimental uncertainty.

Attempts were made to extract the nascent CO vibrational distribution by fitting the entire set of CO(v) signals with an exact mechanism which consisted of the branching steps for production of each vibrational state along with rate constants for v-v transfer between adjacent states. This was done using the kinetic modeling program ACUCHEM[60] to generate the temporal profiles for each CO(v) state and graphically superimposing them on the corresponding signals. The individual rate constants in the mechanism were iteratively adjusted (manually) to agree with the data, starting with the highest observed level and working downward. While qualitative agreement with the data could be obtained in this way, the method did not yield useful quantitative results. The individual CO(v) absorption signals, which are the result of differences in populations between adjacent states, were strongly dependent on the input values of the v-v energy transfer rate constants. A complete set of these rate constants could in principle be obtained by flash kinetic spectroscopy. However, in their absence this fitting algorithm was too cumbersome for useful purposes. It was also difficult to obtain data on all CO(v) states under the same experimental conditions (i.e., ketene and O_2 pressures, UV fluence, etc.), so that an entire matrix of CO(v) signals which could be fit simultaneously with the same mechanism was never acquired. Finally, the CO(v = 1) signal needs to be generated with 13-C ketene as a precursor because the reaction of ketene with OH (see sections III.B.4 and III.B.5) also produces CO(v = 1). For these reasons, the branching ratios for production of CO(v = 2, 3) were obtained from the magnitude of the t = 0 CO(v) signals (*vide supra*) and the rate data for CO(v = 0, 1) was analyzed as described below.

Integration of the rate equations arising from reactions 11-14 yields eq 15, which describes the temporal evolution of the CO(v = 0, j") absorption signal, $I_{\{CO(v=0,\ j'')\}}$, which is proportional to the difference of populations [CO(v = 0, j")] - [CO(v = 1, j')].

$$I_{\{CO(v=0,j'')\}} \propto [CH_2]_0 f_{j''}^{v=0} \left\{ X + Y + \frac{\left(1 + \frac{f_{j'}^{v=1}}{f_{j''}^{v=0}}\right) Y k_1[O_2]}{k_{14}[CH_2{}^{13}CO] - k_1[O_2]} \exp(-k_{14}[CH_2{}^{13}CO]t) - \left(X + Y \frac{k_{14}[CH_2{}^{13}CO] + \frac{f_{j'}^{v=1}}{f_{j''}^{v=0}} k_1[O_2]}{k_{14}[CH_2{}^{13}CO] - k_1[O_2]} \right) \exp(-k_1[O_2]t) \right\} \quad (15)$$

In eq 15, X and Y are the branching ratios for the channels leading to CO(v = 0) and CO(v ≥ 1): $X = k_{11}/k_1$ and $Y = k_{12}/k_1$. The f_j^v represent the fraction of molecules with a specific rotational quantum number within a vibrational level assuming a Boltzmann distribution at 298 K. The CO(v = 0) signal rise is thus composed of two exponentials which depend on the O_2 and ketene pressures used in an experiment. Three experiments were performed in order to extract accurate values for the parameters in eq 15.

Under conditions where $k_1[O_2] >> k_{14}[CH_2{}^{13}CO]$, the two exponentials are temporally resolved and it is possible to extract from a fit to the data that 33 ± 3% of the CO is produced vibrationally excited. Figure 1.12a displays a typical data trace and fit. In fitting for the relative vibrational branching ratios, it was found to be most efficient to fix the value of $k_1[O_2]$ to be the product of the published rate constant and the measured $[O_2]$. Since the sum (X + Y) is known

from the total CO yield (0.34), the CO vibrational branching ratios can be calculated to be 0.23 and 0.11 for X and Y, respectively. (Due to the presence of [CO(v ≥ 2)] the actual value of X is underestimated and of Y is overestimated, but in the absence of a conclusive vibrational distribution the stated values were used in the subsequent analysis. Based on the amplitude of the CO(v ≥ 2) signals and the behavior of the CO(v = 1) signal, the correct values are likely X = 0.25 ± 0.04 and Y = 0.09 ± 0.02.)

While trying to establish a value for k_{14}, it became necessary to examine the CO(v = 1) profiles more closely. As a result, the rate constant for v-v transfer from CO(v = 1) to $CH_2{}^{13}CO$, k_{18}, was determined to be $(1.1 \pm 0.1) \times 10^{-11}$ cm^3 $molecule^{-1}$ s^{-1} by fitting several CO(v = 1) decays as a function of ketene pressure, Figure 1.13. The fit function included contributions to the CO(v = 1) signal from [CO(v ≥ 2)], as derived from a scheme analogous to that for CO(v = 0):

$$CH_2 + O_2 \rightarrow CO(v = 0) + \text{products} \quad (11)$$

$$CH_2 + O_2 \rightarrow CO(v = 1) + \text{products} \quad (16)$$

$$CH_2 + O_2 \rightarrow CO(v \geq 2) + \text{products} \quad (17)$$

$$CH_2 + O_2 \rightarrow \text{other products not CO} \quad (13)$$

$$CO(v = 1) + CH_2{}^{13}CO \rightarrow CO(v = 0) + CH_2{}^{13}CO(v_2 = 1) \quad (18)$$

$$CO(v \geq 2) + CH_2{}^{13}CO \rightarrow CO(v = 1) + CH_2{}^{13}CO(v_2 \geq 1) \quad (19).$$

The analytically integrated form of the differential equations arising from the above mechanism yielded eq 20 for the temporal dependence of the CO(v = 1) signal assuming that $k_{19} = 2k_{18}$ (a harmonic oscillator approximation).

$$[CH_2]_0(\kappa_1-\kappa_{18})^{-1}(\kappa_1-2\kappa_{18})^{-1}\{(\kappa_1(\kappa_{17}-\kappa_{16})+\kappa_{18}(\kappa_{17}+2\kappa_{16}))\exp(-\kappa_1 t) - 3\kappa_{17}(\kappa_1-\kappa_{18})\exp(-2\kappa_{18}t) + (\kappa_1(\kappa_{16}+2\kappa_{17})-\kappa_{18}(2\kappa_{16}+4\kappa_{17}))\exp(-\kappa_{18}t)\} \quad (20)$$

In eq 20, the κ_i represent pseudo-first order rate constants, e.g., $\kappa_{16} = k_{16}[O_2]$ and $\kappa_{18} = k_{18}[CH_2{}^{13}CO]$. The CO(v=1) traces were fit to eq 20 leaving the parameter κ_1 fixed at the known value using the published rate constant. From the ratio $k_{17}/(k_{16} + k_{17})$ obtained from the fits, it appears that 25 ± 3% of the vibrationally excited CO product molecules are produced with more than 1 quantum of vibrational excitation. This is consistent with the measured amplitudes of the CO(v = 2, 3) signals discussed above.

The observed slow component of the CO(v = 0) rise in Figure 1.12a is somewhat slower (10%) than expected from simple first-order kinetics of CO(v = 1) due to the influence of CO cascading down from higher levels (v ≥ 2). Thus, the more empirical rate constant, $k_{14} = 1.0 \times 10^{-11}$ cm^3 molecule^{-1} s^{-1}, for the decidedly non-elementary reaction 14 was obtained from the slow portion of CO(v = 0) rises under high $[O_2]/[CH_2CO]$ conditions and used in subsequent fits for k_1. The resulting k_1 was found to be fairly insensitive to the value of k_{14} used.

With all parameters already determined except $k_1[O_2]$, it was then possible to fit each low $[O_2]/[CH_2CO]$ CO(v = 0) rise trace to eq 15 with all parameters fixed except $k_1[O_2]$ and an amplitude scaling factor. A typical data trace and non-linear least squares fit is displayed in Figure 1.12b. For each trace, a value of $k_1[O_2]$ is thus extracted; a plot of $k_1[O_2]$ *vs.* $[O_2]$ for many traces (Figure 1.14) gives the rate constant $k_1 = (3.0 \pm 0.1) \times 10^{-12}$ cm^3 molecule^{-1} s^{-1}, where the uncertainty is the 95% confidence interval of the linear fit to the slope.

The systematic errors in the rate constant measurements and analysis procedure are estimated to be smaller than 10% thus giving a methylene loss rate constant, as measured from CO production, of $k_1 = (3.0 \pm 0.4) \times 10^{-12}$ cm^3 $molecule^{-1}$ s^{-1}. Because this rate constant is within 7% of the published rate constant for removal of $^3CH_2$ by O_2, it can be concluded that the data is consistent with CO being produced directly in reaction 1.

III.B.3. CO_2 Branching Ratio and Production Rate

The yield of CO_2, using $^{13}CH_2CO$ as a precursor, is given by

$$\frac{\left[{}^{13}CO_2\right]_{t>>\tau}}{\left[{}^{12}CO\right]_{phot}}$$

and is calculated analogously to the CO yield. Table 1.3 summarizes the results of the CO_2 experiments which indicate that the branching ratio for the production of CO_2 is $0.40^{+0.09}_{-0.07}$; the uncertainty contains contributions from random (±0.05) and systematic $\left(^{+0.04}_{-0.02}\right)$ errors. The observed $CO_2(v_1 = v_2 = v_3 = 0)$ product exhibited a significant induction period (20 - 30 μs) which disappeared upon addition of SF_6. The induction period is attributed to vibrational excitation of the nascent CO_2 product, which undergoes subsequent vibrational relaxation. If the CO_2 rise experiments are performed such that $[O_2]/[SF_6] << 1$, the temporal profile is well fit by a single exponential rise function, whose rate is interpreted as $k_1[O_2]$. A plot of a typical data trace and fit is displayed in Figure 1.15. The measured rates of production $k_1[O_2]$ are plotted against $[O_2]$ in Figure 1.16, yielding a rate constant $k_1 = (3.8 \pm 0.3) \times 10^{-12}$ cm^3 $molecule^{-1}$ s^{-1}, where the

uncertainty is the 95% confidence interval for the linear fit to the slope. Estimating the systematic errors in the rate constant measurement to be less than 10%, the resulting value of $k_1 = (3.8 \pm 0.6) \times 10^{-12}$ cm^3 $molecule^{-1}$ s^{-1} is obtained for the methylene loss rate constant, as measured from CO_2 production. Since this rate constant falls within the error limits of the published rate constant for removal of CH_2 by O_2, the data is consistent with CO_2 being produced directly in reaction 1.

III.B.4. H_2CO Branching Ratio

H_2CO can be produced in reactions 1c and 1i. On the timescales of interest in this experiment (t < 200 μs), the secondary reaction of the OH formed in reactions 1a and 1d with ketene is an additional source of CO and, indirectly, H_2CO:

$$OH + CH_2CO \rightarrow CO + CH_2OH \qquad (21)$$

$$CH_2OH + O_2 \rightarrow H_2CO + HO_2 \qquad (22).$$

Isotopic substitution of ^{13}C in the carbonyl position of ketene leads exclusively to ^{13}CO as a secondary reaction product (no ^{12}CO is observed so that reaction 21 does not interfere with the CO yield measurements). To distinguish the fraction of the total H_2CO signal produced directly in reactions 1c and 1i from that formed in reaction 22, 2-methyl-2-butene was used to scavenge the OH before it reacted with ketene:[61]

$$OH + \text{2-methyl-2-butene} \rightarrow \text{products not } H_2CO \qquad (23).$$

A simplified mechanism consisting of reactions 1a, 1c, 1d, and 1i, followed by reactions 21-23 leads to eq 24 for the dependence of the H_2CO yield on the 2-methyl-2-butene scavenger pressure.

$$\frac{[H_2CO]}{[CH_2]_0} = \frac{k_{1c} + k_{1i}}{k_1} + \frac{k_{1a} + k_{1d}}{k_1}\left(1 + \frac{k_{23}[\text{scavenger}]}{k_{21}[\text{ketene}]}\right)^{-1} \qquad (24)$$

In Figure 1.17, the H_2CO yield data (taken at 0.78 torr ketene, 1.2 torr O_2, and 5.2 torr Ar) is plotted against the relative scavenger to ketene pressure. The data was empirically normalized for 2-methyl-2-butene collisional quenching of ketene and collisional broadening of H_2CO by measuring the attenuation of the CO photolysis yield (from ketene) and the H_2CO peak absorption coefficient as a function of added 2-methyl-2-butene. Superimposed on the data is a non-linear least squares fit to eq 24 which indicates that the branching ratio for production of H_2CO, $(k_{1c} + k_{1i})/k_1$, is 0.14 ± 0.03, with the uncertainty containing an estimate of possible systematic errors (±0.01). This analysis implicitly assumes that all of the methylene reacts with O_2. However, the recombination of CH_2, reaction 7, accounts for the loss of 13% of the initial methylene concentration, leading to a smaller observed yield of H_2CO. Numerically integrating the rate equations for the competition between CH_2 recombination and reaction with O_2 and varying the branching ratio for H_2CO production until agreement with the measured yield was obtained lead to a corrected H_2CO yield of 0.16 ± 0.04. Additionally, from the fit to the data it could be determined from the ratio k_{23}/k_{21} that OH reacts 6 ± 2 times faster with 2-methyl-2-butene than with ketene, where the uncertainty is 2σ from the fit.

III.B.5. OH Branching Ratio

OH can be produced in reactions 1a and 1d. The fact that OH reacts with ketene to give CO and H_2CO (via reactions 21 and 22) allows for an indirect probe of its yield in reaction 1. The branching ratio for OH production, $(k_{1a} + k_{1d})/k_1$, could be extracted from a fit of eq 24 to the data in Figure 1.17 and suggests that OH is the major (85 ± 20%) coproduct of CO (or HCO). The ^{13}CO produced in reaction 21, subsequent to the photolysis of $CH_2{}^{13}CO$ in the presence of O_2, provides an alternative measure of the yield of OH, see Figure 1.18. Preliminary data show that the secondary ^{13}CO amplitude is 0.32 ± 0.06 (2σ) of the photolytic amplitude (after correction for the loss of ^{13}CO due to C-atom exchange), which indicates that the OH/CO ratio from reaction 1 is 0.94 ± 0.25.

IV. Discussion

IV.A. Comparison to other studies

These results represent the first time-resolved quantitative determination of the absolute yields of the principal C-containing products from reaction 1. The products observed in these experiments account for 90^{+14}_{-12}% of the initial methylene formed. An effort was made to detect HCOOH as a possible additional reaction product, but no signal was observed. Based on the measured peak absorption coefficient of the line probed, an upper limit of 0.01 can be placed on the branching ratio k_{1j}/k_1 at 20 torr total pressure. We thus believe that all the C-containing product yields have been measured and that experimental error led to the slightly low total

product yield. The reported error bars indicate that a total yield of 1.0 is within our 95% confidence interval.

The observed $CO:CO_2$ ratio is in qualitative agreement with the results of Rowland and coworkers[13] who reported those products in approximately equal amounts. They did not, however, detect any H_2CO formation. On the other hand, Dombrowsky and Wagner determined the $CO:CO_2$ ratio to be 4:1 by IR emission in their high temperature shock tube studies.[6]

Other studies have noted the formation of formaldehyde or $O(^3P)$ but the yield was believed to be 10% or less. The experiments of Böhland *et al.* relied on the absence of a pronounced difference in the measured rate constant k_1 for two different CH_2 sources to place an upper limit of 10% on the O atom yield.[3] More recently the observed $O(^3P)$ atom profile in a shock wave (1000 - 1800 K) was simulated with a value for $k_{1c}/k_1 = 0.10$.[6] The discrepancy in the H_2CO yield could point to the production of both $O(^3P)$ and $O(^1D)$, since the other studies relied on measurements of $O(^3P)$.

It is conceivable that H_2CO is produced directly in reaction 25 rather than by the two-step process (reactions 21 and 22) described in section III.B.4.

$$OH + CH_2CO \rightarrow H_2CO + HCO \qquad (25)$$

In the presence of O_2, the HCO formed in reaction 25 would rapidly generate HO_2 and CO, thus leading to the same products obtained from reaction 21 followed by reaction 22. The reaction of OH with ketene has been examined by a number of investigators[62-65] with reported

rate constants in the range (1.2 - 3.3) $\times 10^{-11}$ cm^3 $molecule^{-1}$ s^{-1}. Little is known about the products, but CO, CO_2, and H_2CO have been detected.[62] The uncertainty in the secondary H_2CO formation mechanism does not affect the results presented here because the OH was scavenged by 2-methyl-2-butene. However, more work would be required to elucidate the products of the reaction between OH and ketene. Our measured ratio $k_{23}/k_{21} = (6 \pm 2)$, together with the recommended[61] rate constant $k_{23} = 8.7 \times 10^{-11}$ cm^3 $molecule^{-1}$ s^{-1}, is consistent with the literature values for k_{21} mentioned above.

From the yield of secondary H_2CO and from the secondary ^{13}CO formed subsequent to the photolysis of $CH_2{}^{13}CO$ in O_2, it is evident that OH is produced as the major coproduct of CO (or HCO). The indirectly measured ratio of [OH]/[CO] is ~0.9 ± 0.2 from both measurements. An upper limit of 0.3 was placed on the yield of OH producing channels by Bley *et al.* but secondary chemistry in their system prevented an accurate determination.[4] Shaub *et al.* fit the vibrational distribution of CO formed in reaction 1 with a statistical model which indicated that 70% of the CO product may be formed in reaction 1a and only 30% in reaction 1b.[39] The indirect results obtained in this work are consistent with both previous studies, and suggest that the OH yield in reaction 1 is comparable to the CO yield. At high temperatures (1000 - 1800 K) the OH yield was measured to be less than 5% by direct absorption. The possibility of slow vibrational relaxation of excited OH could not be ruled out, so that the actual yield may be higher.[6] Together with the $CO:CO_2$ ratio of 4:1, the high temperature data require that the reaction dynamics be different than

at room temperature, the molecular reaction channel 1b becoming the dominant pathway.

IV.B. Reaction mechanism

Considering the available energy of a CH_2O_2 complex formed in reaction 1, it is evident that facile interconversion can occur among the CH_2O_2 isomers on the ground state surface. A meaningful theoretical prediction of the branching ratios is difficult due to the large excess energy available for decomposition of a CH_2O_2 complex and the absence of data necessary to estimate state densities for the complexes and total state counts for the various transition states. A plausible overall mechanism involves formation of a complex by end-on addition, singlet or triplet **I**, or insertion, **III**. H_2CO and $O(^3P)$ or $O(^1D)$ are readily formed via **I**. At the available energy, **I** converts readily to **III** by cyclization followed by ring opening. Complex **III** may eliminate an H atom and then the remaining HC(O)O could decompose to H + CO_2 or rearrange to HOCO which fragments to give H + CO_2 and OH + CO. Alternatively, **III** may undergo an H atom migration to form highly excited formic acid, **IV**, which could fragment into HCO + OH, H + HC(O)O, or H + HOCO. A detailed *ab initio* investigation would be useful in helping to elucidate which of the possible CH_2O_2 decomposition pathways lead to the observed products.

These experiments measure the yield of all channels which result in production of CO, CO_2, and H_2CO on the μs timescale. Using careful kinetic analysis, we conclude that the results are consistent with CO and CO_2 being produced directly in reaction 1. The present experimental sensitivity and temporal resolution do not allow for a

distinction to be made between CO and CO_2 arising as direct products from the unimolecular dissociation of CH_2O_2 intermediates **I - IV** (simple elimination or concerted triple dissociation) or from the subsequent fragmentation of an excited product species such as HCO, HOCO, or HC(O)O. With the energy available to be released into these product channels, sequential dissociation can occur before a collision occurs. For the purposes of combustion modeling, the intermediacy of a transient species whose lifetime is shorter than a collisional period is of no importance. The possibility does exist, however, that the secondary reactions 26-28 of stable radical intermediates are sources of the observed CO and CO_2.

$$HCO + O_2 \rightarrow CO + HO_2 \quad (26)$$

$$HOCO + O_2 \rightarrow CO_2 + HO_2 \quad (27)$$

$$HC(O)O + O_2 \rightarrow CO_2 + HO_2 \quad (28)$$

The measured rate constants of reactions 26 and 27, $k_{26} = 5.5 \times 10^{-12}$ cm^3 molecule^{-1} s^{-1} [66] and $k_{27} = (1.9 \pm 0.2) \times 10^{-12}$ cm^3 molecule^{-1} s^{-1} [67] are not greatly different from k_1. Nothing is known about reaction 28 but its rate constant should be of comparable magnitude. A mechanism for production of CO or CO_2 via consecutive reactions yields a temporal profile characterized by two time constants and a discernible induction period. A single exponential rise profile describing the direct production of CO or CO_2 in a pseudo-first order process (as used in this work) would not fit the data accurately, and would result in smaller production rates. We have tried simulating the CO_2 rise data as if it were composed of both a direct (reactions 1f and

1g) and a secondary (reaction 1e followed by reaction 27) mechanism. From the simulation and our measured S/N ratios, we estimate an upper limit of 0.15 for the relative contribution of reaction 27 to the measured CO_2 yield. More precisely, the ratio $k_{1e}/(k_{1e} + k_{1f} + k_{1g} + k_{1h}) \leq 0.15$. In the absence of a reliable experimental value of k_{28}, a similar argument can not be presented for a mechanism containing reaction 28. The measured CO(v = 0) product rise profiles were complicated by the presence of vibrational excitation, but the data is adequately modeled by a mechanism consisting of direct production including vibrational excitation. However, the intermediacy of reaction 26 can not be ruled out. Experiments that directly probe the HCO, HOCO, and HC(O)O radicals should be carried out to conclusively establish or rule out their presence in this system. Notwithstanding the uncertainty about the intermediacy of several radicals, in the O_2 rich environment characteristic of combustion processes, the same CO and CO_2 product yields reported here should obtain.

V. Conclusion

The stable C-containing products from the reaction $^3CH_2 + O_2$ have been measured using an infrared diode laser flash kinetic spectrometer. The branching steps of reaction 1 are key inputs to the modeling of acetylene combustion.[68,69] This study reaffirms the accepted near-equality of CO and CO_2 yields and identifies the modest production of H_2CO in reaction 1. The measured product yields suggest that $(k_{1a} + k_{1b} + k_{1d})/k_1 = 0.34 \pm 0.06$ (CO production), $(k_{1e} + k_{1f} + k_{1g} + k_{1h})/k_1 = 0.40^{+0.09}_{-0.07}$ (CO_2 production), and $(k_{1c} + k_{1i})/k_1 = 0.16 \pm 0.04$ (H_2CO production). Based on indirect evidence obtained

in this work and on previous studies, it appears likely that the OH yield in this system, $(k_{1a} + k_{1d})/k_1$, is 0.30 ± 0.05. An upper limit was placed on the HCOOH yield: $k_{1j}/k_1 \leq 0.01$. Because the O-atom yield is equivalent to that of H_2CO, the only remaining uncertainty is the branching between molecular and atomic hydrogen production.

VI. References

(1) Laufer, A. H. Rev. Chem. Intermed. **1981**, 4, 225, and references therein.

(2) Darwin, D. C.; Young, A. T.; Johnston, H. S.; Moore, C. B. J. Phys. Chem. **1989**, 93, 1074.

(3) Böhland, T.; Temps, F.; Wagner, H. Gg. Ber. Bunsenges. Phys. Chem. **1984**, 88, 455.

(4) Bley, U.; Temps, F.; Wagner, H. Gg.; Wolf, M. Ber. Bunsenges. Phys. Chem. **1992**, 96, 1043.

(5) Vinckier, C.; Debruyn, W. J. Phys. Chem. **1979**, 83, 2057.

(6) Dombrowsky, Ch.; Wagner, H. Gg. Ber. Bunsenges. Phys. Chem. **1992**, 96, 1048.

(7) Kafafi, S. A.; Martinez, R. I.; Herron, J. T. in Modern Models of Bonding and Delocalization; Liebman, J. F., Greenberg, A., Eds.; VCH: New York, 1988; p 283.

(8) Melius, C. F., 1988, Personal Communication.

(9) Ruscic, B.; Schwarz, M.; Berkowitz, J. J. Chem. Phys. **1989**, 91, 6780.

(10) Kim, E. H.; Bradforth, S. E.; Arnold, D. W.; Neumark D. M., to be published.

(11) Baulch, D. L.; Cox, R. A.; Hampson, R. F.; Kerr, J. A.; Troe, J.; Watson, R. T. J. Phys. Chem. Ref. Data **1980**, 9, 295.

(12) Langford, A. O.; Petek, H.; Moore, C. B. J. Chem. Phys. **1983**, 78, 6650.

(13) Rowland, F. S., Lee, P. S.-T.; Montague, D. C.; Russell, R. L. J. Chem. Soc., Faraday Disc. **1972**, 53, 111.

(14) Ha, T.-K.; Kühne, H.; Vaccani, S.; Günthard, Hs. H. Chem. Phys. Lett. **1974**, 24, 172.

(15) Harding, L. B.; Goddard, W. A. J. Am. Chem. Soc. **1978**, 100, 7180.

(16) Karlström, G.; Engström, S.; Jönsson, B. Chem. Phys. Lett. **1979**, 67, 343.

(17) Cremer, D.; Schmidt, T.; Gauss, J.; Radhakrishnan, T. P. Angew. Chem. Int. Ed. Engl. **1988**, 27, 427.

(18) Bach, R. D.; Andrés, J. L.; Owensby, A. L.; Schlegel, H. B.; McDouall, J. J. W. J. Am. Chem. Soc. **1992**, 114, 7207.

(19) Karlström, G.; Roos, B. O. Chem. Phys. Lett. **1981**, 79, 416.

(20) Cimiraglia, R.; Ha, T.-K.; Günthard, Hs. H. Chem. Phys. Lett. **1982**, 85, 262.

(21) Dupuis, M.; Lester, W. A. J. Chem. Phys. **1984**, 80, 4193.

(22) Goddard, J. D.; Yamaguchi, Y.; Schaefer, H. F. J. Chem. Phys. **1992**, 96, 1158.

(23) Francisco, J. S. J. Chem. Phys. **1992**, 96, 1167.

(24) Criegee, R. Angew. Chem. Int. Ed. Engl. **1975**, 14, 745.

(25) Horie, O.; Moortgat, G. K. Atmospheric Environment **1991**, 25A, 1881.

(26) Atkinson, R.; Finlayson, B. J.; Pitts, J. N. J. Am. Chem. Soc. **1973**, 95, 7592.

(27) Kühne, H.; Vaccani, S.; Bauder, A.; Günthard, Hs. H. Chem. Phys. **1978**, 28, 11.

(28) Su, F.; Calvert, J. G.; Shaw, J. H. J. Phys. Chem. **1980**, 84, 239.

(29) Brouard, M.; O'Mahony, J. Chem. Phys. Lett. **1988**, 149, 45.

(30) Suto, M.; Wang, X.; Lee, L. C. J. Phys. Chem. **1988**, 92, 3764.

(31) Ebata, T.; Amano, T.; Ito, M.; J. Chem. Phys. **1989**, 90, 112.

(32) Singleton, D. L.; Paraskevopoulos, G.; Irwin, R. S. J. Phys. Chem. **1990**, 94, 695.

(33) Möller, D., Atmospheric Environment **1988**, 22, 2607.

(34) Strachan, A. N.; Noyes, W. A. J. Am. Chem. Soc. **1954**, 76, 3258.

(35) Holroyd, R. A.; Noyes, W. A. J. Am. Chem. Soc. **1956**, 78, 4831.

(36) Russell, R. L.; Rowland, F. S. J. Am. Chem. Soc. **1968**, 90, 1671.

(37) Eberius, K. H.; Hoyermann, K.; Wagner, H. Gg. Symp. (Int.) Combust., 14th **1972**, 147.

(38) Hsu, D. S. Y.; Lin, M. C. Int. J. Chem. Kin. **1977**, 9, 507.

(39) Shaub, W. M.; Hsu, D. S. Y.; Burks, T. L.; Lin, M. C. Symp. (Int.) Combust., 18th **1981**, 811.

(40) Vinckier, C.; Debruyn, W. Symp. (Int.) Combust., 17th **1978**, 623.

(41) Lee, Y.-P.; Pimentel, G. C. J. Chem. Phys. **1981**, 74, 4851.

(42) Hatakeyama, S.; Bandow, H.; Okuda, M.; Akimoto H. J. Phys. Chem. **1981**, 85, 2249.

(43) Horie, O.; Moortgat, G. K. Ber. Bunsenges. Phys. Chem. **1992**, 96, 404.

(44) Knyazev, V. D.; Arutyunov, V. S.; Vedeneev, V. I. Sov. J. Chem. Phys. **1992**, 11, 762.

(45) Darwin, D. C., Ph.D. Dissertation, University of California, Berkeley, 1989.

(46) Lovejoy, E. R.; Alvarez, R. A.; Moore, C.B. Chem. Phys. Lett. **1990**, 174, 151.

(47) Lovejoy, E. R., Kim, S. K.; Alvarez, R. A.; Moore, C. B. J. Chem. Phys. **1991**, 95, 4081.

(48) Bitto, H.; Chen, I.-C.; Moore, C. B. J. Chem. Phys. **1986**, 85, 5101.

(49) For a general discussion of semiconductor lasers , see Hecht, J. Understanding Lasers; Howard W. Sams & Co.: Indianapolis, 1988, Ch. 6.

(50) Harward, C. N.; Hoell, J. M. App. Optics **1979**, 18, 3978.

(51) Rodriguez, M.; Alvarez, R. A. Rev. Sci. Instrum. **1992**, 63, 4014.

(52) Guelachvili, G.; Rao, K. N. Handbook of Infrared Standards; Academic: San Diego, 1986.

(53) Bréchignac, C.; Johns, J. W. C.; McKellar, A. R. W.; Wong, M. J. Mol. Spect. **1982**, 96, 353.

(54) Chackerian, C.; Guelachvili, G.; Tipping, R. H. J. Quant. Spectrosc. Rad. Transfer **1983**, 30, 107.

(55) Spence, R.; Wild, W. J. Chem. Soc. (London) **1935**, 338.

(56) Nesbitt, D. J.; Petek, H.; Foltz, M. F.; Filseth, S. V.; Bamford, D. J.; Moore, C. B. J Chem. Phys. **1985**, 83, 223.

(57) Chen, I.-C.; Moore, C. B. J. Phys. Chem. **1990**, 94, 263.

(58) Chen, I.-C.; Moore, C. B. J. Phys. Chem. **1990**, 94, 269.

(59) Hayden, C. C.; Neumark, D. M.; Shobatake, K.; Sparks, R. K.; Lee, Y. T. J. Chem. Phys. **1982**, 76, 3607.

(60) Braun, W.; Herron, J. T.; Kahaner, D., National Bureau of Standards, 1986.

(61) Atkinson, R. Chem. Rev. **1985**, 85, 69.

(62) Faubel, C.; Wagner, H. Gg.; Hack, W. Ber. Bunsenges. Phys. Chem. **1977**, 81, 689.

(63) Hatakeyama, S.; Honda, S.; Washida, N.; Akimoto, H. Bull. Chem. Soc. Jpn. **1985**, 58, 2157.

(64) Brown, A. C.; Canosa-Mas, C. E.; Parr, A. D.; Wayne, R. P. Chem. Phys. Lett. **1989**, 161, 491.

(65) Oehlers, C.; Temps, F.; Wagner, H. Gg.; Wolf, M. Ber. Bunsenges. Phys. Chem. **1992**, 96, 171.

(66) DeMore, W. B.; Sander, S. P.; Golden, D. M.; Molina, M. J.; Hampson, R. F.; Kurylo, M. J.; Howard, C. J.; Ravishankara, A. R. Chemical Kinetics and Photochemical Data for Use in Stratospheric Modeling, Evaluation Number 9; JPL Publication 90-1, 1990.

(67) Petty, J. T.; Harrison, J. A.; Moore, C. B., submitted to J. Phys. Chem..

(68) Miller, J. A.; Mitchell, R. E.; Smooke, M. D.; Kee, R. J. Symp. (Int.) Combust., 19th **1982**, 181.

(69) Miller, J. A.; Kee, R. J.; Westbrook, C. K. Annu. Rev. Phys. Chem. **1990**, 41, 345.

Table 1.1. Ab Initio values for relative energies of CH_2O_2 isomers and barriers to their interconversion and decomposition.

Species[a]	Relative E (kcal/mol)	Method	Ref
I(singlet)	37	SCF-MO	14
	35	GVB-CI	15
	33	MC-CI	16
	35	BAC-MP4	8
	31	MP4(SDQ)/6-31G*	17
	44	UMP4/6-31G*	7
	29	QCISD/6-31G*	18
I(triplet)	58	MP4	8
	62	GVB-CI	15
III(singlet)[b]	6	MC-CI	16
	15	GVB-CI	15
	10	UMP4/6-31G*	7
Barriers[c]			
I → **II**	22-24	MC-SCF	19
	23	MP4(SDQ)/6-31G*	17
	19	QCISD/6-31G*	18
I(^{3}A) → H_2CO+O(^{3}P)	1.4	BAC-MP4	8
II → CO_2 + H_2	63[d]	CI	20
II → **IV**	> 85	CI	20
III($^1A_1$) → **IV**($^1A_1$)	<13	MC-HF	21
III($^3B_2$) → **IV**($^3A_1$)	>30	MC-HF	21
IV → CO + H_2O	68	DZ+P CCSDT-1	22
	63	e	23
IV → CO_2 + H_2	71	DZ+P CCSDT-1	22
	65	e	23

[a] Relative E values for ground state energies assume dioxirane (**II**) is energy zero

b Singlet and triplet are nearly degenerate (refs 15 and 21)

[c] Barriers are relative to species on left side of arrow

[d] $\angle OCO = 157^o$

[e] PMP4/6-311++G**//UMP2/6-311G**

Table 1.2. Summary of CO yield measurements

Ketene Isotope[a]	P_{ketene}, torr	P_{Ar}, torr	P_{O_2}, torr	P_{total}, torr	Fluence, mJ cm^{-2}	Photolysis Reference[a]	CO Yield
12,13	0.29	19.6	2.5	22.4	33	12,13	0.352
12,13	0.29	19.6	3.3	23.2	33	12,13	0.362
12,13	1.00	19.0	3.0	23.0	33	12,13	0.340
12,13	0.15	19.3	3.0	22.4	54	12,13	0.310
12,13	0.30	0	19.7	20.0	33	12,12	0.351
12,13	0.30	0	19.8	20.1	33	12,12	0.329
12,13	0.10	0	7.9	8.0	33	12,12	0.341
13,12	0.26	19.0	3.9	23.2	30	13.12	0.310
13,12	0.15	20.0	3.8	23.9	30	13,12	0.335

[a] 12,12 = CH_2CO; 12,13 = $^{12}CH_2{}^{13}CO$; 13,12 = $^{13}CH_2{}^{12}CO$

[b] The yield is corrected for C-atom exchange and isotopic impurities as follows: for a 12,12 reference experiment, the corrected yield is $(0.989[^{12}CO]_{reaction}/0.935[CO]_{photolysis}) - 0.065/0.935$; and for a 12,13 experiment, e.g., the yield is $([^{12}CO]_{reaction}/[^{13}CO]_{photolysis}) - 0.065/0.935$.

Table 1.3. Summary of CO_2 yield data

$P(^{13}CH_2CO)$ torr	$P(O_2)$, torr	$P(SF_6)$, torr	$[CO_2]_{t=\infty}$, mtorr	$[CH_2]_0$,[a] mtorr	Yield
0.123	0.514	6.49	0.0467	0.112	0.410
0.113	1.02	5.03	0.0410	0.105	0.385
0.098	1.35	5.60	0.0344	0.0857	0.398

[a] Determined from photolysis of a normal ketene sample, accounting for loss of $[^{13}CH_2]_0$ due to exchange and isotopic impurities by multiplying by 0.935/0.989

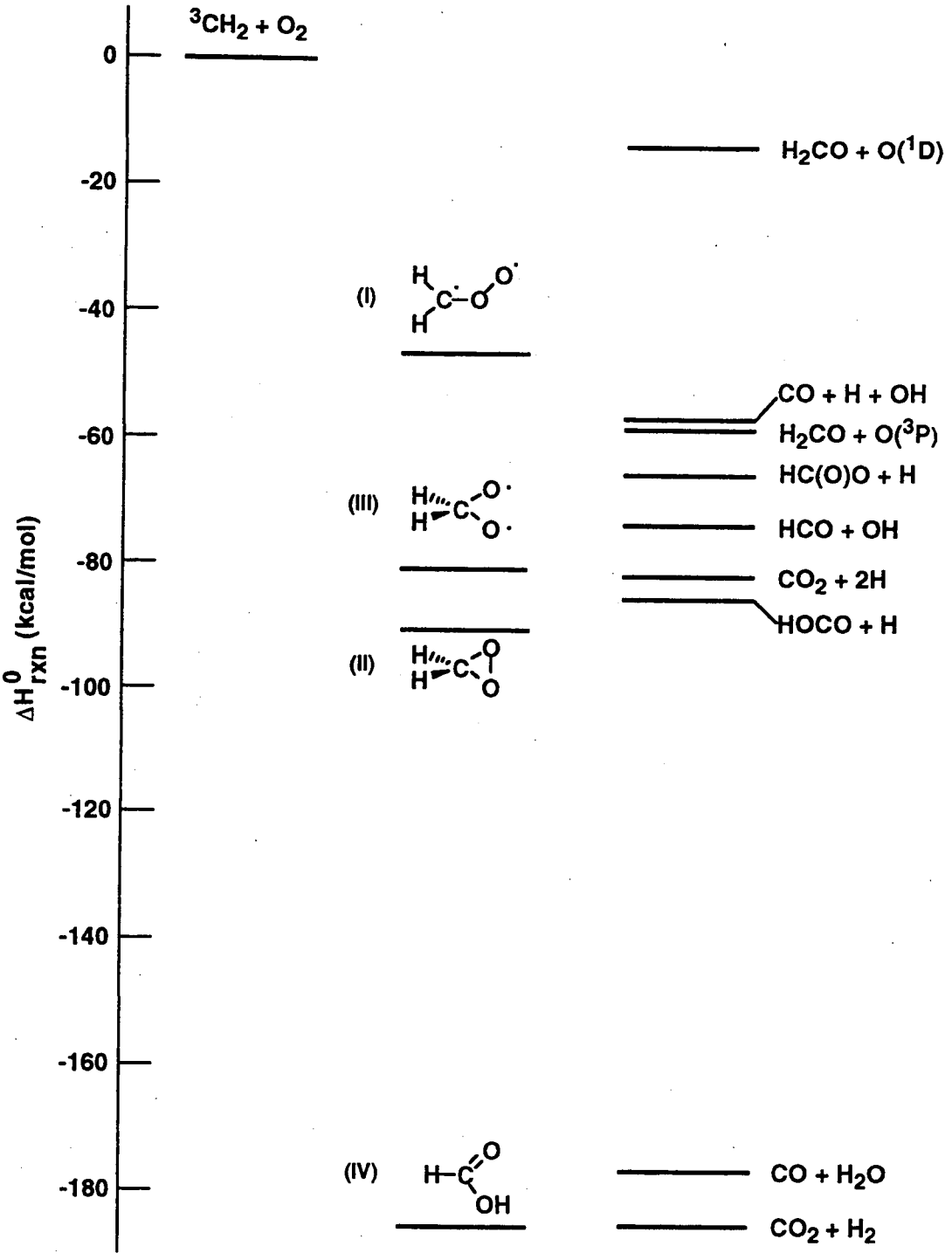

Figure 1.1. Calculated reaction enthalpies (T=298K) for some possible product channels and intermediates in reaction 1. $\Delta H_f^0(298)$ values for CH_2O_2 isomers were taken from the recommended values in ref 7, for $^3CH_2$ from ref 8 (92.8 kcal/mol), for HOCO from ref 9 (-52.5 kcal/mol), for HC(O)O from ref 10 (-30 kcal/mol), and for all other product species from ref 11.

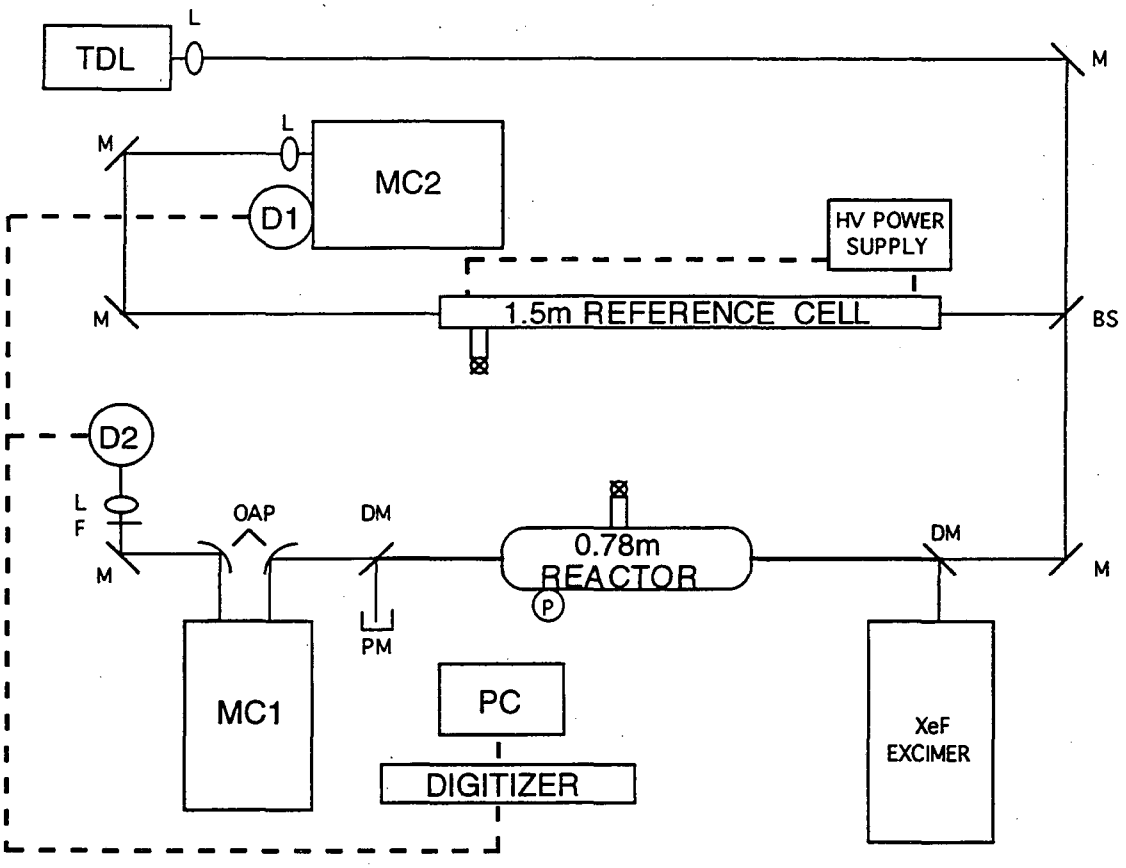

Figure 1.2. Schematic of infrared diode laser flash kinetic spectrometer. L = lens, M = mirror, DM = dichroic mirror, BS = beamsplitter, P = capacitance manometer, MC = monochromator, OAP = off-axis parabolic mirror, F = interference filter, PM = power meter, and D = detector. The dashed lines denote electrical connections.

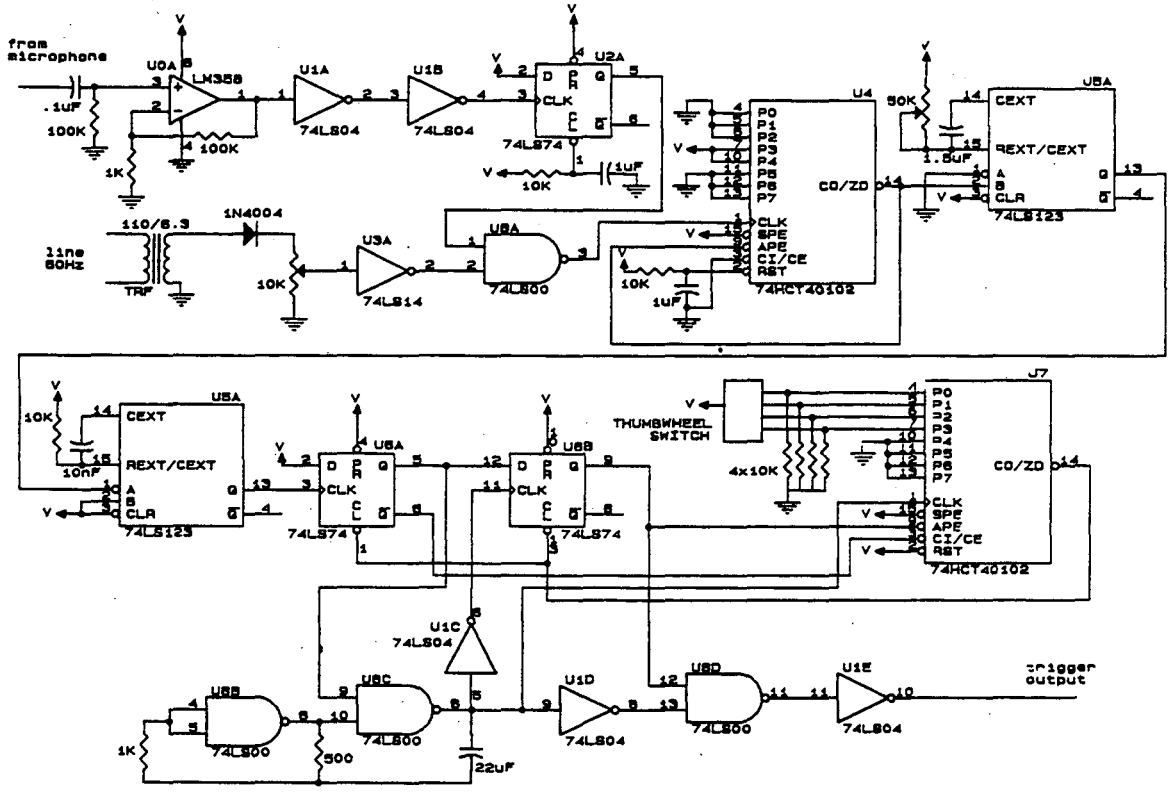

Figure 1.3. Schematic of trigger circuit for flash kinetic data acquisition. The circuit provides a trigger synchronous to the cycle of the cold head piston, and allows for data to be taken during the quiet part of the cold head cycle.

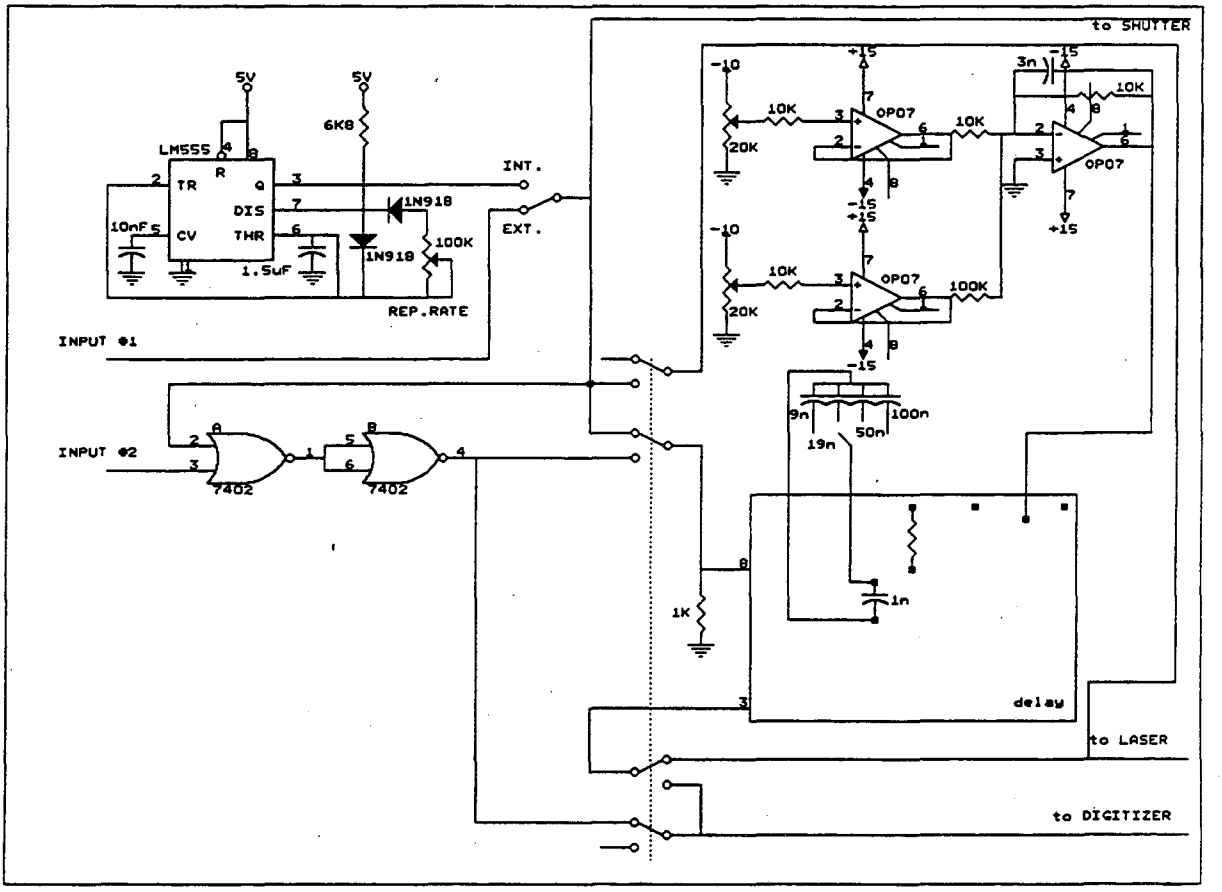

Figure 1.4. Schematic of circuit which generates delays between excimer and digitizer triggers. Provision is made for external (input #1) or internal triggering, an output for triggering an external shutter to block UV beam, and an external input (input #2) which only triggers the digitizer.

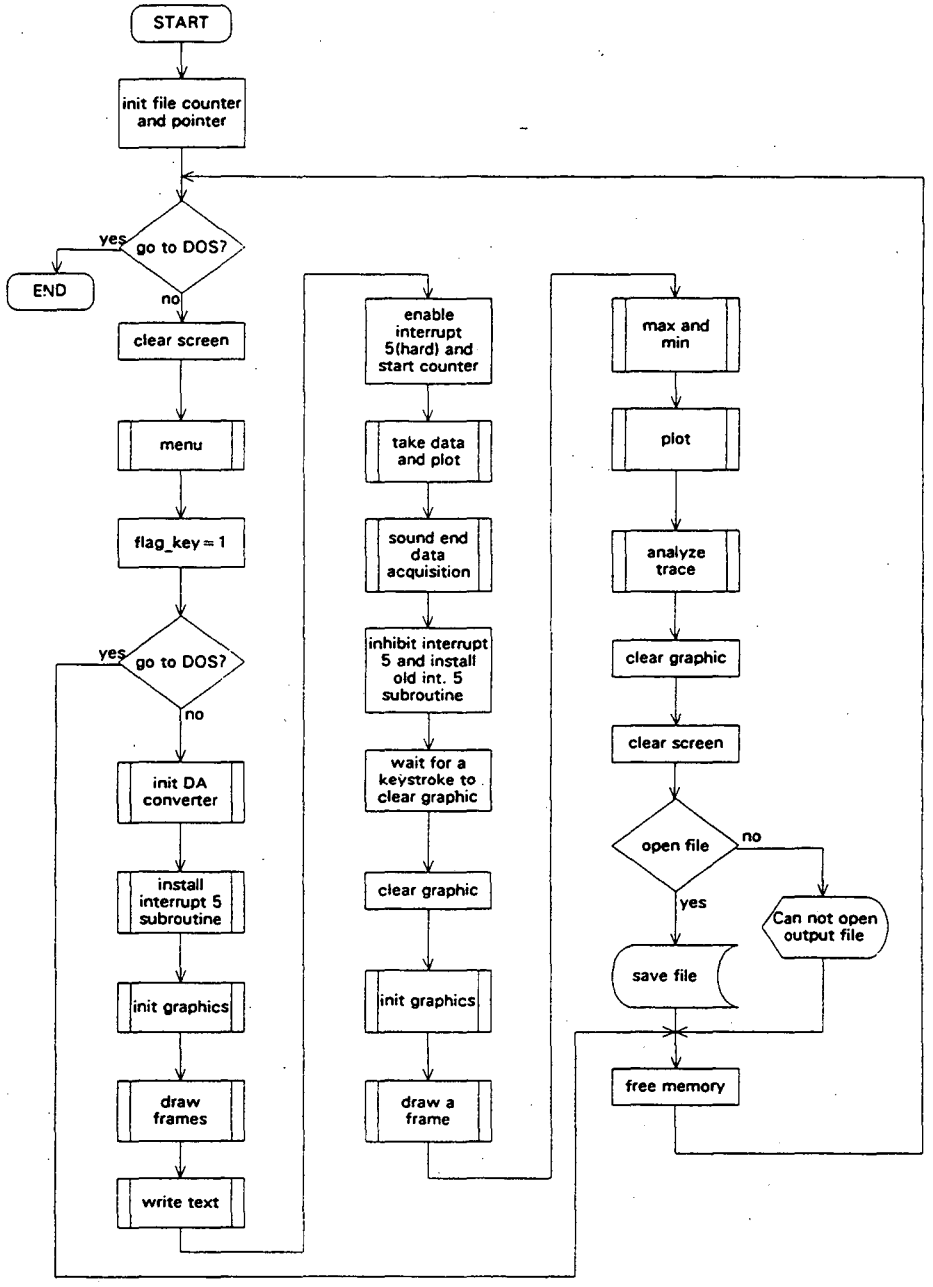

Figure 1.5. Flowchart of the spectral acquisition program FLASH.

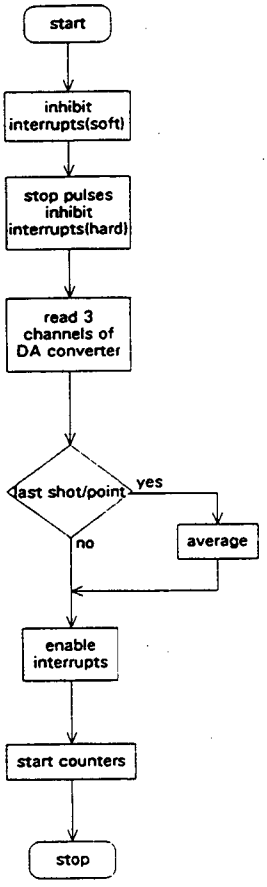

Figure 1.6. Flowchart of the FLASH subroutine which controls the interrupt sequence.

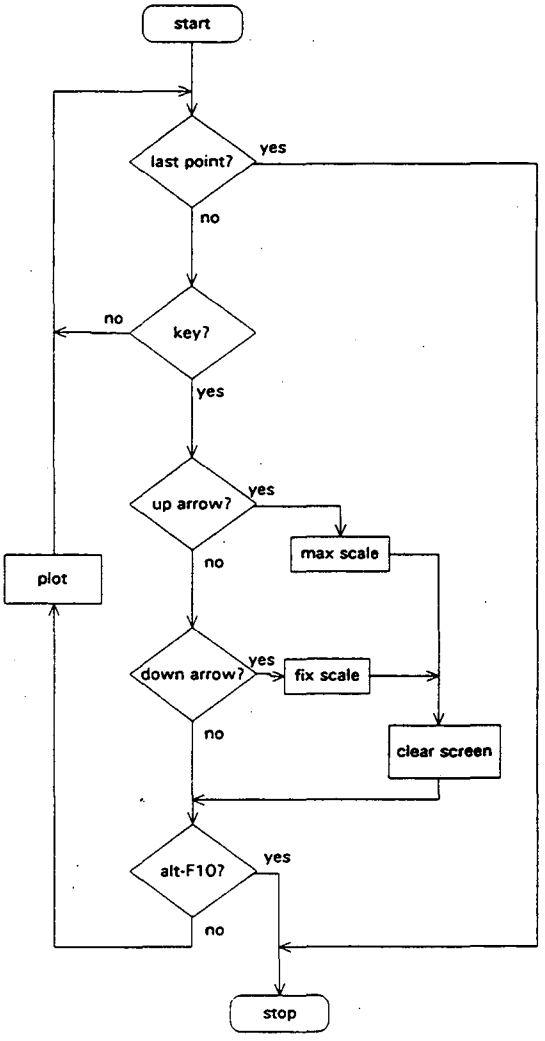

Figure 1.7. Flowchart of the FLASH subroutine which controls the real-time interactive graphics mode.

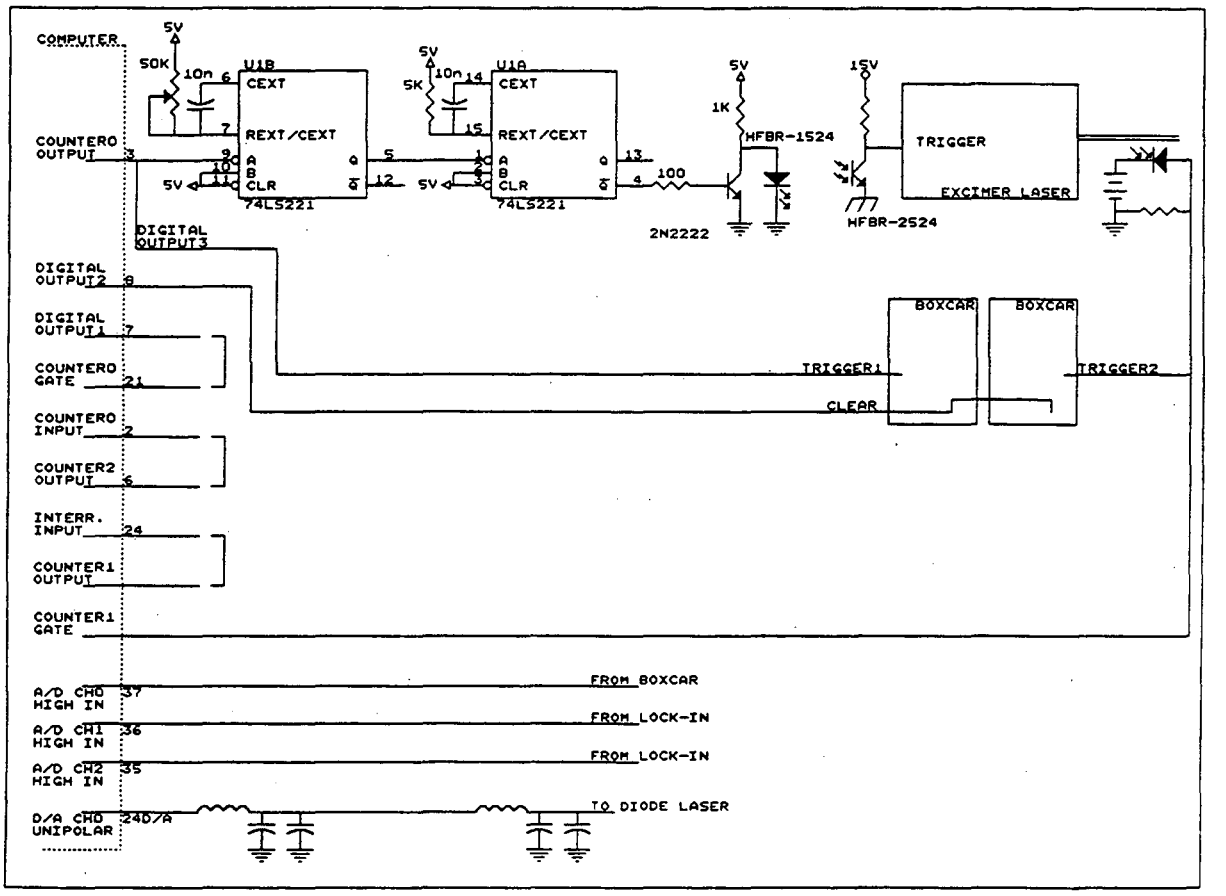

Figure 1.8. Schematic of interface circuit and hardware connections required for spectral acquisition using FLASH.

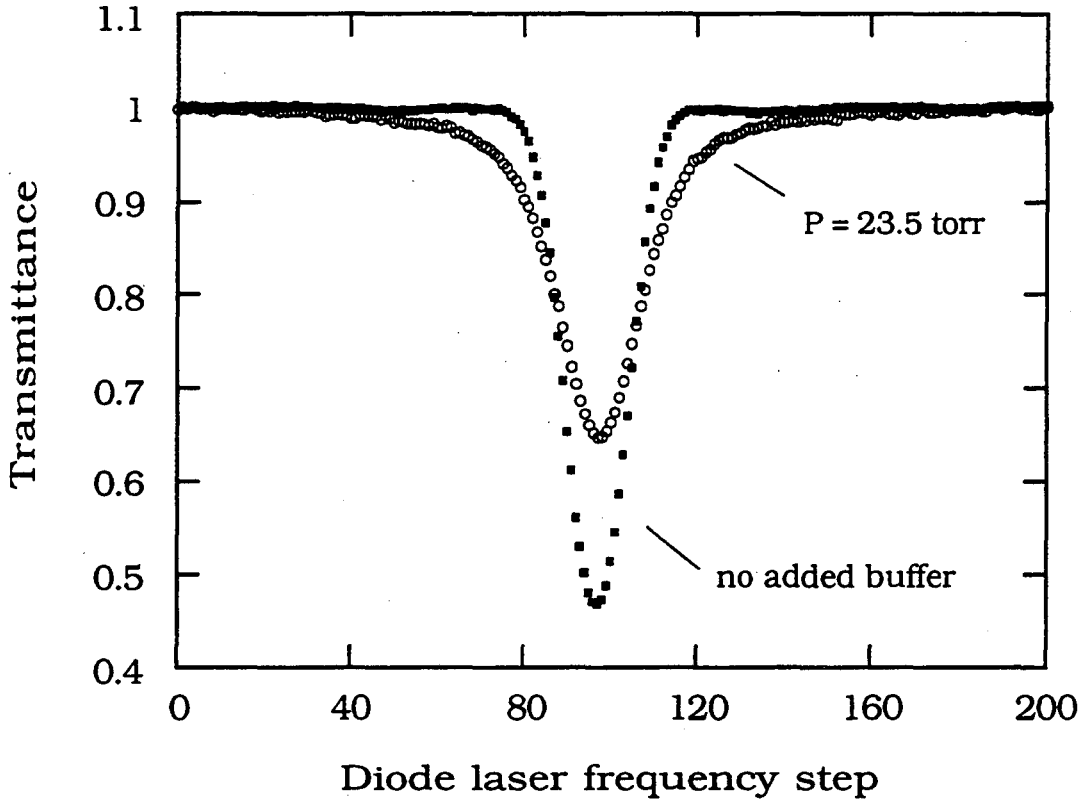

Figure 1.9. Spectrum of ^{12}CO P(14) (9 mtorr) acquired using the spectral scanning routine FLASH. The addition of 23.5 torr of SF_6 buffer collisionally broadens the line and reduces the peak absorption coefficient by a factor of 1.74.

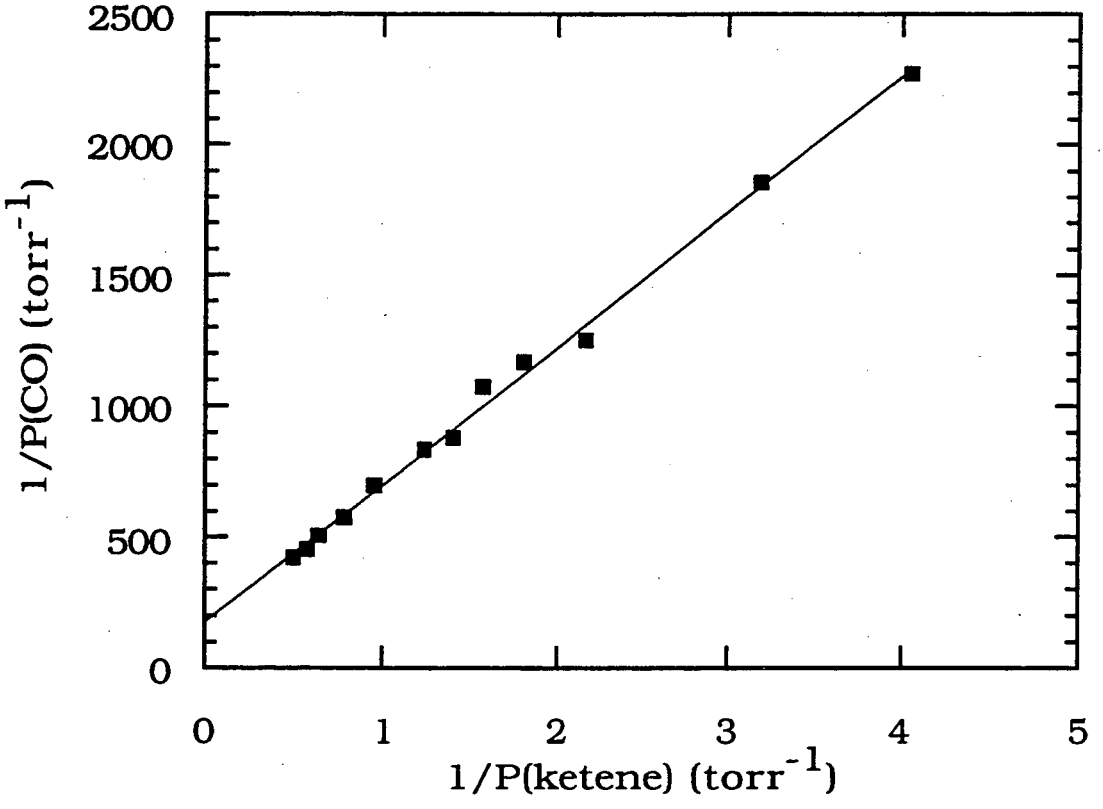

Figure 1.10. Stern-Volmer plot of loss of CO photolysis product due to ketene collisional self-quenching. The linear fit to eq 2 yields a value of $k_5/k_4 = 0.34$ torr^{-1} from the ratio of intercept to slope.

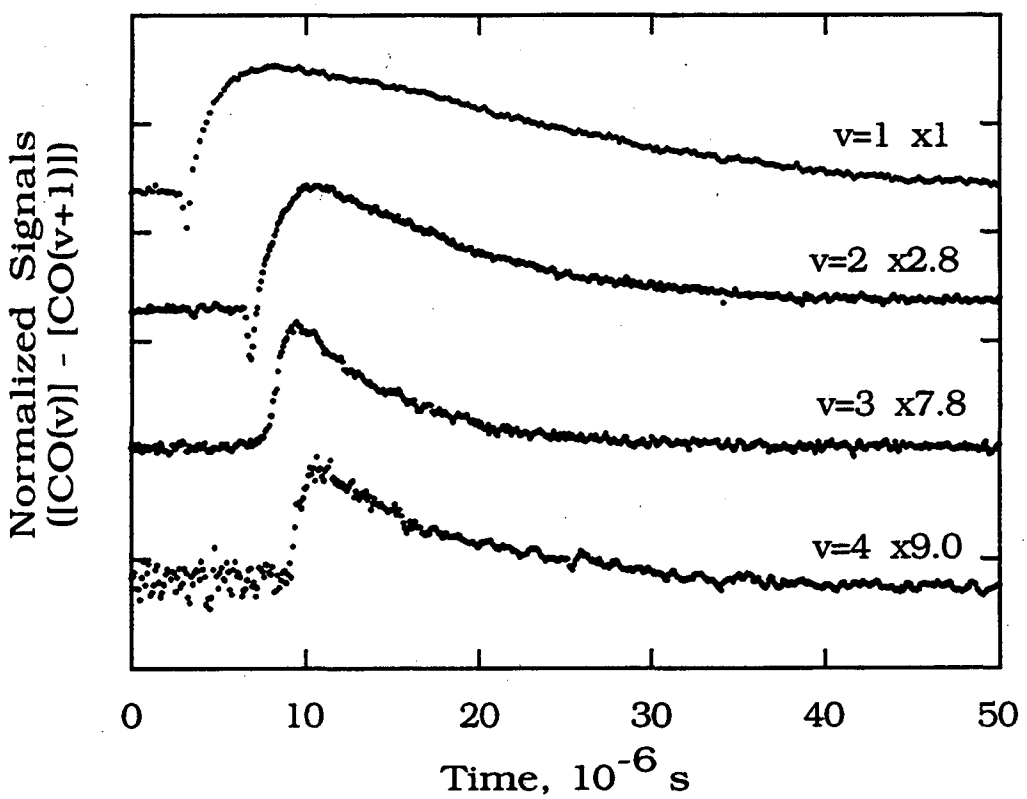

Figure 1.11. Rise profiles of CO(v=1-4) normalized relative to CO(v=1) signal. Conditions: CO(v=1), R(7) probe of photolysis (40 mJ cm^{-2}, 96 pulses averaged) of 0.19 torr $CH_2{}^{13}CO$ in 8.0 torr O_2; CO(v=2), P(9) probe of photolysis (40 mJ cm^{-2}, 160 pulses averaged) of 0.18 torr ketene in 6.9 torr O_2; CO(v=3), R(5) probe of photolysis (80 mJ cm^{-2}, 160 pulses averaged) of 0.15 torr ketene in 19.8 torr O_2; CO(v=4), R(9) probe of photolysis (80 mJ cm^{-2}, 160 pulses averaged) of 0.15 torr ketene in 20.0 torr O_2.

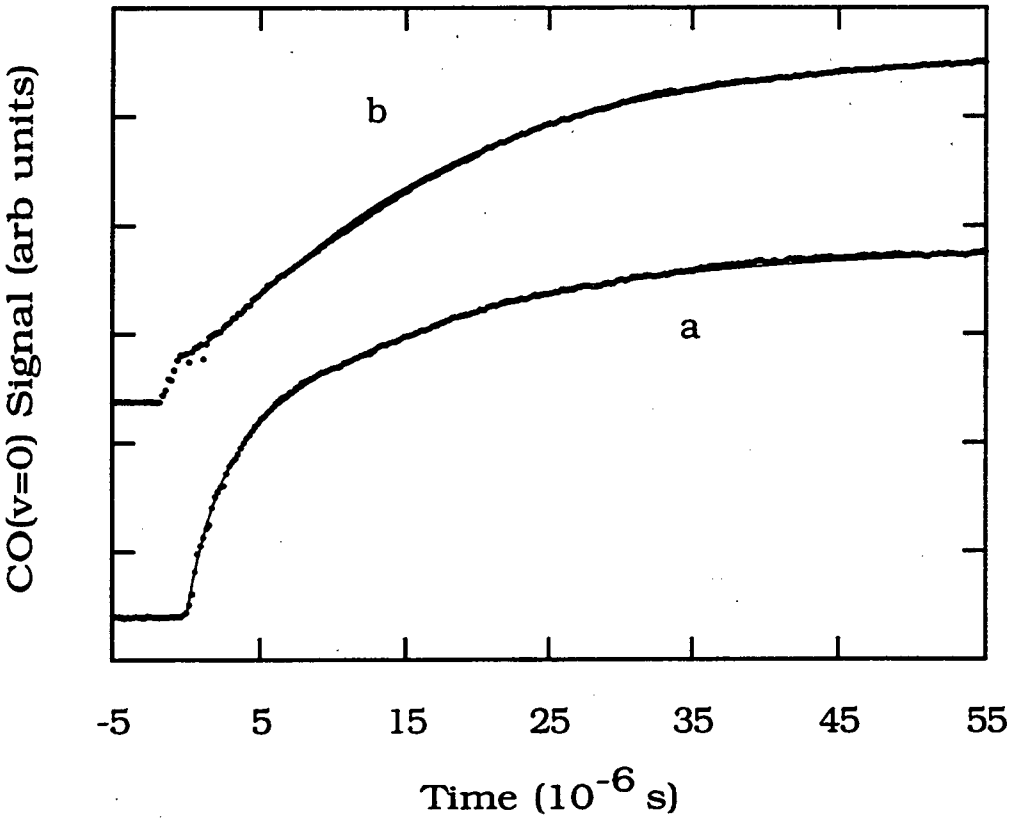

Figure 1.12. Typical $^{12}CO(v = 0)$ rise profiles and fits to eq 15. Conditions: a) 0.20 torr $CH_2{}^{13}CO$, 4.8 torr O_2, 9.1 torr Ar; b) 1.08 torr $CH_2{}^{13}CO$, 0.62 torr O_2, 7.4 torr Ar. The laser pulse energy was 40 mJ cm^{-2} and the line probed was R(11) where $f^{1}_{12}/f^{0}_{11} = 0.89$. The point at which time = 0 is arbitrarily offset, and the fast initial rise in trace b is due to ^{12}CO from C-atom exchange and isotopic impurities. The fit parameters were: a) $k_{14}[CH_2{}^{13}CO] = 6.17 \times 10^4\ s^{-1}$ with $k_1[O_2]$ fixed at $5.01 \times 10^5\ s^{-1}$; b) $k_1[O_2] = 6.20 \times 10^4\ s^{-1}$ with $k_{14}[CH_2{}^{13}CO]$ fixed at $3.67 \times 10^5\ s^{-1}$.

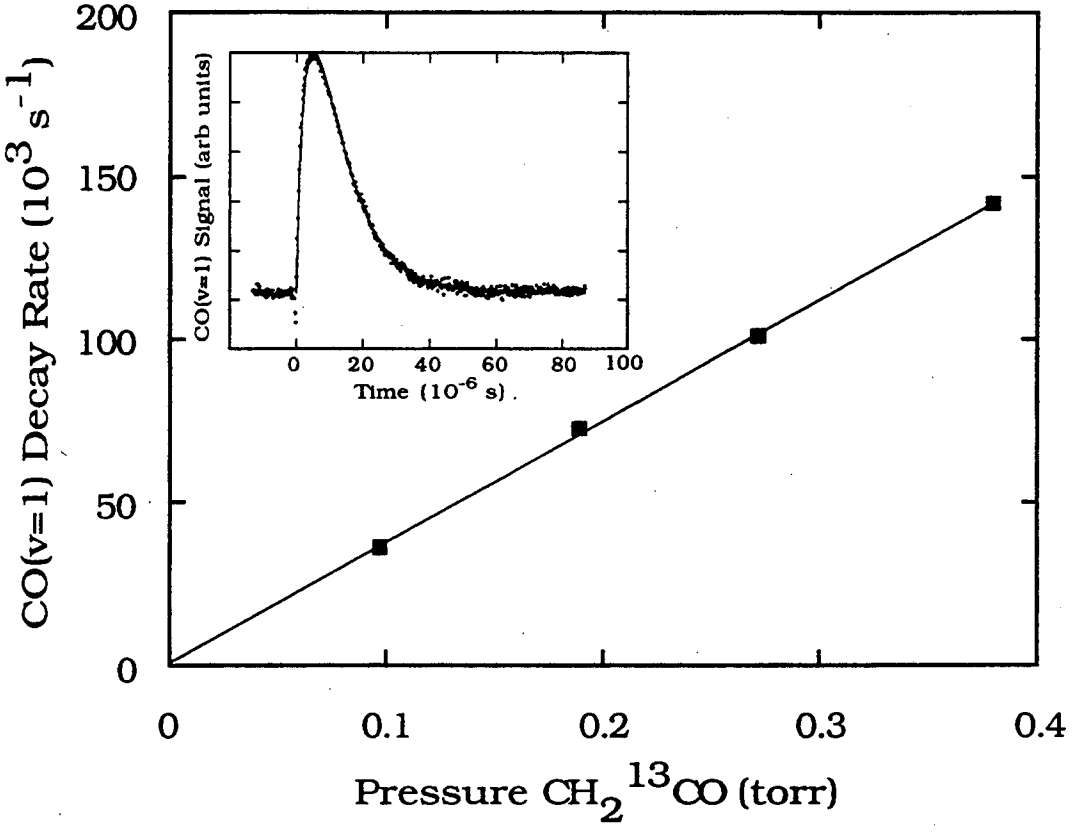

Figure 1.13. Plot of measured CO(v = 1) decay rate *vs.* $CH_2{}^{13}CO$ pressure. The slope of the least squares line yields a value of $k_{18} = (1.1 \pm 0.1) \times 10^{-11}$ cm^3 $molecule^{-1}$ s^{-1}. The inset displays a sample decay trace obtained by probing R(7) of $^{12}CO(v = 1)$ in the photolysis (40 mJ cm^{-2}) of a mixture of 0.27 torr $CH_2{}^{13}CO$ and 7.8 torr O_2. The superimposed fits to the v = 1 data include contributions from CO(v ≥ 2) and indicate that 25% of the vibrationally excited product molecules are produced with more than 1 quantum of vibrational energy. A value of $k_{18}[CH_2{}^{13}CO] = 1.03 \times 10^5$ s^{-1} was obtained from the fit, with $k_1[O_2]$ fixed at 8.15×10^5 s^{-1}.

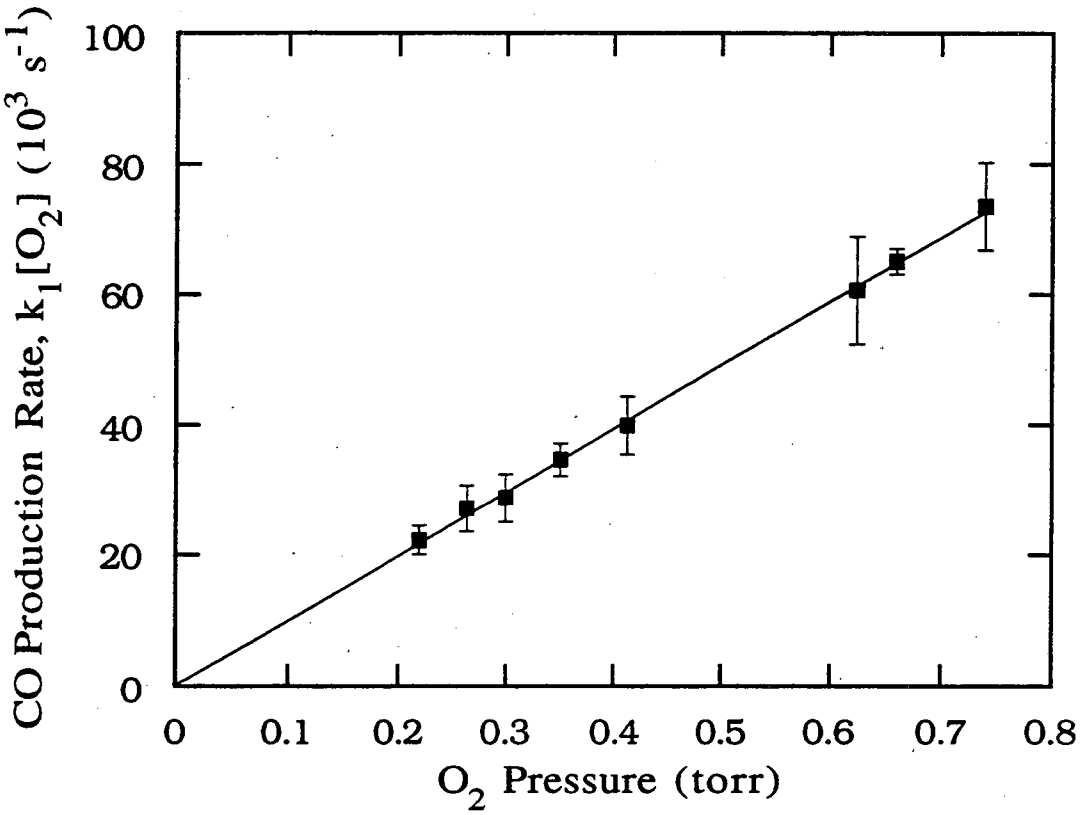

Figure 1.14. Plot of observed rate of CO production, $k_1[O_2]$, *vs.* $[O_2]$. The individual rates were extracted from a fit of eq 15 to low $[O_2]/[CH_2{}^{13}CO]$ CO(v = 0) traces as described in the text. The error bars represent the 95% confidence levels for the mean of 4-7 traces. The slope of the linear least-squares fit to the data indicates that the rate constant for CO production, k_1, is $(3.0 \pm 0.1) \times 10^{-12}$ cm^3 $molecule^{-1}$ s^{-1}.

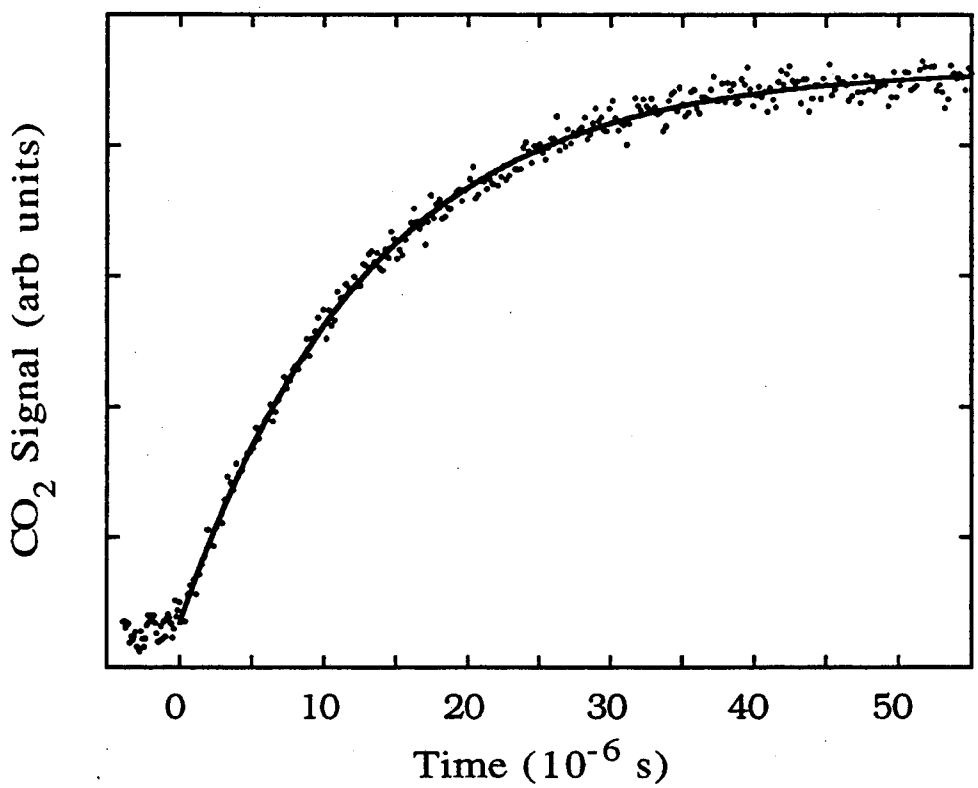

Figure 1.15. Sample $^{13}CO_2$ rise and superimposed fit to a single exponential rise function. The measured rise rate is 7.72×10^4 s^{-1}. Conditions: R(8) probe of $^{13}CO_2$ resulting from the photolysis (25 mJ cm^{-2}) of a mixture of 0.19 torr $^{13}CH_2CO$, 0.64 torr O_2, and 13.9 torr SF_6; 96 traces were co-added; and time = 0 corresponds to the beginning of the fit curve.

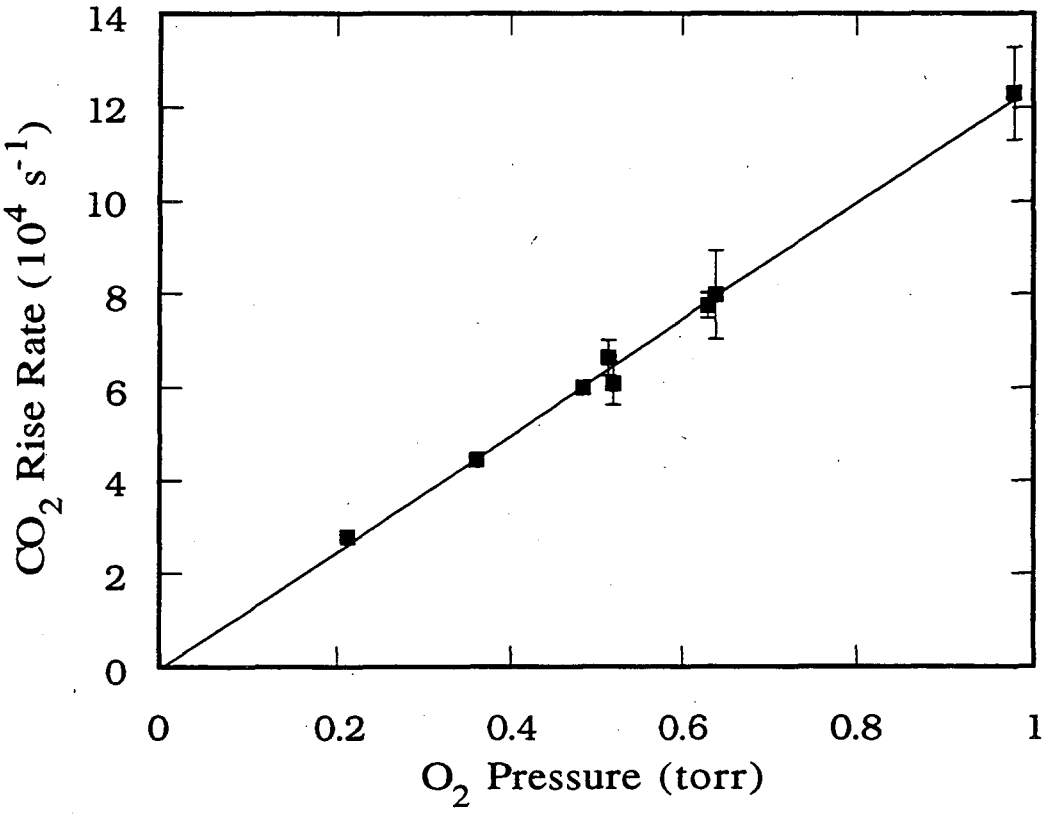

Figure 1.16. Plot of measured $^{13}CO_2$ production rates *vs.* $[O_2]$. The slope of the linear least-squares fit to the data indicates a rate constant for $^{13}CO_2$ production of $(3.8 \pm 0.3) \times 10^{-12}$ cm^3 $molecule^{-1}$ s^{-1}.

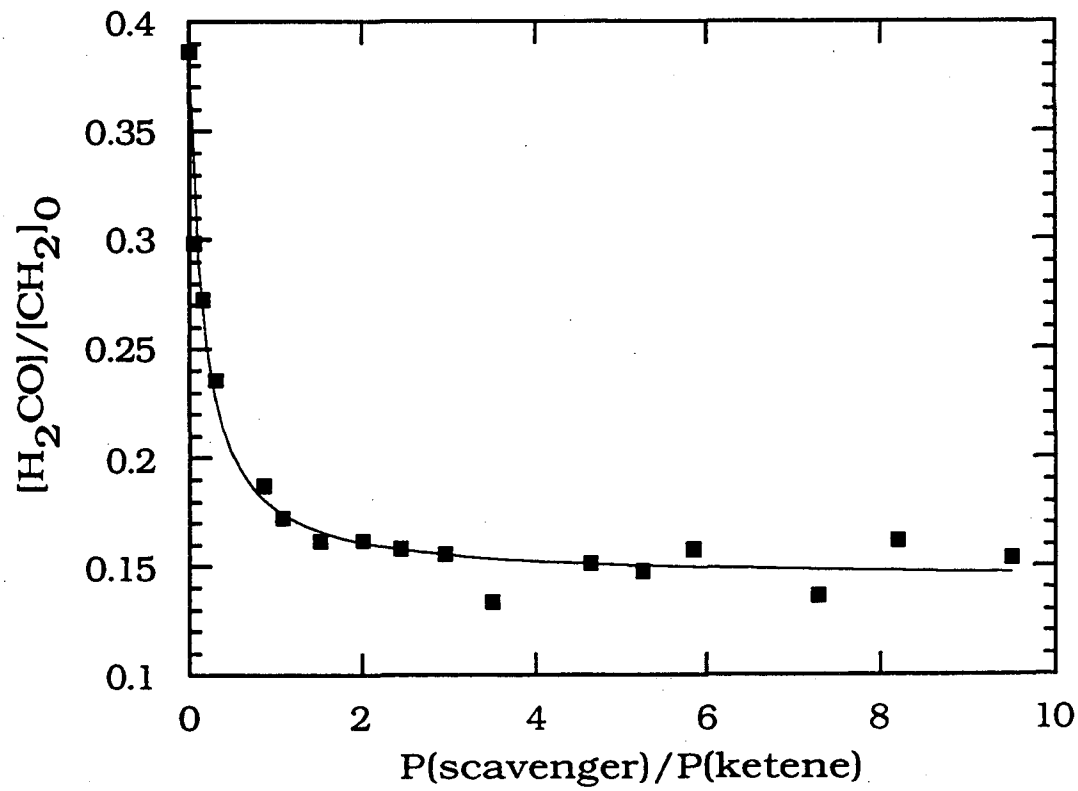

Figure 1.17. Plot of H_2CO yield *vs.* relative 2-methyl-2-butene to ketene pressure. The nonlinear least squares fit of eq 24 to the data indicates that the yield for direct production of H_2CO in reaction 1 is 0.14 ± 0.03, that OH reacts 6 ± 2 times faster with 2-methyl-2-butene than with ketene, and suggests that OH is produced in comparable amounts to CO. See text for corrections to the H_2CO yield resulting from the loss of CH_2 due to recombination.

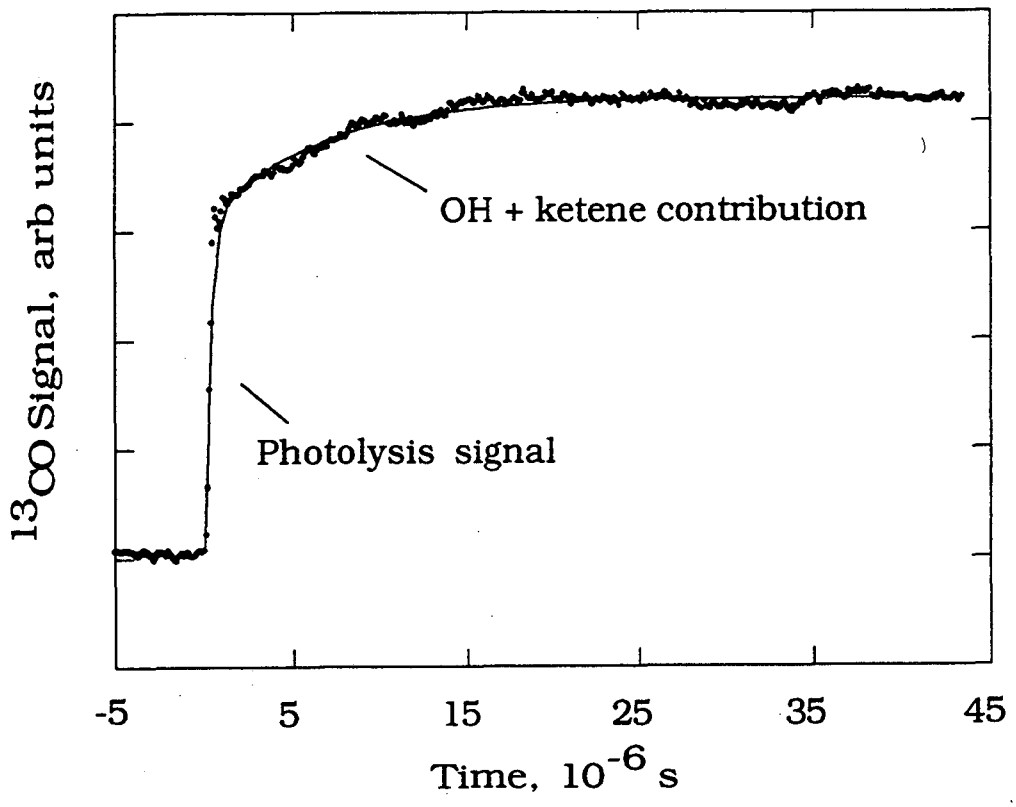

Figure 1.18. ^{13}CO R(20) signal resulting from the photolysis (30 mJ cm^{-2}) of 0.29 torr $CH_2{}^{13}CO$ in 3.3 torr O_2 and 19.7 torr Ar. The slowly rising, secondary component is due to the reaction of OH with ketene, reaction 21. The biexponential fit to the data suggests that the ratio of the secondary amplitude to the photolysis amplitude is 0.38. The photolysis amplitude should be adjusted for losses due to C-atom exchange (see text).

Chapter 2. Quantum yield for production of CH_3NC in the photolysis of CH_3NCS

I. Introduction

Methyl isothiocyanate ($CH_3NCS \equiv$ MITC) is widely used in agriculture as a soil fumigant in various formulations; it is a toxic substance which irritates the skin and mucous membranes.[1] In 1991, 2.1×10^4 metric tons of metam-sodium, which decomposes in the soil to yield MITC, were used in the United States:[2]

$$\underset{\textbf{metam-sodium}}{CH_3NHCS_2^-Na^+} \rightarrow \underset{\textbf{MITC}}{CH_3NCS} + NaHS$$

The California Policy Seminar lists metam-sodium 4th in its priority ranking of high profile pesticides, based on 1990 data on applied volumes.[3] Because of its high vapor pressure (12.8 ± 0.5 torr at 297 K), MITC can enter the troposphere by spray drift during application or subsequent volatilization. Estimating that ~60% of the applied dosage of metam-sodium is emitted as MITC into the air,[4] ~10^4 metric tons of MITC were released into the atmosphere in 1991. For comparison, this amount represents ~0.04% of the total anthropogenic emissions of SO_x and NO_x in the U.S. in 1987.[5] While the relative total amount of MITC released into the atmosphere may seem small, local concentrations of MITC may be sufficiently high to warrant concern. The threshold for toxicity of MITC is presently under debate within the state regulatory agencies; however, it is believed that MITC levels above 1 ppb may cause discomfort in some members of the population.[6] Concentrations as high

as 3 to 242 μg m^{-3} (1 to 81 ppb) have been measured at sites downwind from fields injected with metam-sodium.[7,8] It is expected that the application of metam-sodium by sprinkler irrigation in warm weather (as is typical in the San Joaquin Valley) should lead to even higher ambient MITC concentrations.[8]

The persistence of pollutants in the atmosphere may pose health and environmental hazards. In order to assess the potential risks arising from the use of toxic substances, it is useful to know the dominant mechanism and the rate for their removal from the atmosphere. The fate of species in the troposphere is determined by some combination of i) photodissociation; ii) chemical removal, e.g., reaction with other trace species such as OH and O_3; and iii) physical removal, such as through dry deposition or rainout.[9] Figure 2.1 schematically illustrates the possible fates of a pesticide in the environment. This study deals with the fundamental photochemistry of MITC and indicates that solar photodissociation could be the chief removal pathway of MITC.

The ultraviolet (UV)[10-12] and vacuum-ultraviolet (VUV)[13,14] absorption spectra of MITC have been previously reported, but the spectrum at wavelengths with significant solar flux ($\lambda \geq 295$) has not been measured. The NCS radical in various electronic states has been detected as a product from the UV and VUV photolysis of MITC using a wavelength selected broadband source,[13] synchrotron radiation,[14] and excimer lasers,[15] as well as from electron impact on MITC.[16] The decomposition of MITC in a discharge has been observed to yield NCS[17,18] and CS, CN, and S_2.[18] The distribution of vibrational energy in the NCS fragment[15] and rotational and vibrational energy in the CN fragment[19] resulting from the 248- and 193-nm photolyses of MITC have been reported. The

production of $S(^3P)$ atoms and CH_3NC in solutions of MITC irradiated with 254-nm light has also been reported to occur, with a maximum yield of 45%.[20,21] However, nothing is known about the photolysis of MITC at energies corresponding to the long-wavelength tail of its lowest energy absorption band, and the quantum yields of the photolysis products have not been quantified at any wavelength.

II. Experimental

The UV spectrum of MITC was acquired on an HP 8452 UV/VIS spectrometer with a resolution of 2 nm. An 8.0-cm quartz cell held the sample and the evacuated cell served as the blank for all scans. The 100% transmittance level was determined by averaging the %T values in the 340 - 360 nm range where no signal was detected. All spectra were taken at 298 ± 2 K where σ = Absorbance(base e) / [P(MITC) × (3.25 × 10^{16}) × 8.0], see Appendix 1. Sample pressures were measured with a calibrated 10-torr capacitance manometer (MKS Instruments), and accounting for possible wall loses (adsorption or catalyzed decomposition) are correct to ± 5%. The UV spectrum of MITC, taken in the quartz UV cell, was constant to within 10% over a 19-hour period. Over longer times (3 - 4 days) the absorbance at wavelengths below 310 nm fell by as much as 10% while rising considerably (10 - 30%) for wavelengths between 310 and 350 nm. This suggests the possible slow decomposition of MITC and formation of CS_2, whose near-UV absorption spectrum peaks near 320 nm.[22] The UV spectra were taken within 3 minutes of filling the cell to minimize any such losses.

The diode laser flash kinetic spectrometer is described in detail in Chapter 1. An excimer laser (Lambda Physik, EMG 103 MSC) running on

XeCl was used to photolyze MITC at 308 nm. A diode lasing in the region 2060 - 2190 cm^{-1} with a resolution of 0.0003 cm^{-1} probed the ν_2 band of CH_3NC.[23] Transient changes in the cw infrared laser power of 5 parts in 10^4 could be detected, giving a detection limit for CH_3NC of ~5×10^{11} molecules cm^{-3} per laser shot (S/N ~ 1, in the absence of collisional broadening). All transient yield experiments were performed at T = 298 ± 2 K. Peak absorption coefficients and their attenuation by collisional broadening were determined by scanning the diode laser over a CH_3NC absorption feature, using the program FLASH as described in Chapter 1.

The FTIR analysis of CH_3NC production was performed on a Nicolet 510P at 1-cm^{-1} resolution and averaging over 64 scans. A 15.4-cm long glass cell (inner diameter = 22 mm) sealed with CaF_2 windows held the samples. Spectral analysis was performed using the autosubtract, baseline, and integrate routines of the PC/IR software. Typical precision for the FTIR analyses is estimated to be ± 20% (2σ). Even in the absence of photolysis, the MITC samples decayed considerably in the IR cell over the period of observation (20% loss in 20 minutes, e.g.), but the decay did not lead to production of CH_3NC, and is probably due to some wall loss process. The conditioning of the cell walls, i.e., the substances to which the cell had been exposed, appears to play a role in this decay of MITC. All photolysis/FTIR experiments were performed over similar lengths of time to minimize errors due to loss of MITC.

MITC was obtained from Aldrich with a specified purity of > 97%. However, lot analysis (gas chromatography, Aldrich Technical Services) revealed that our sample was considerably purer (99.6%). The sample was received as a yellowish solid, heated past its melting point (310 K), and transferred with a pipet into an Erlenmeyer flask which was fitted

with a ground glass joint so that it could be adapted with a stopcock and evacuated. The sample was degassed by 3 successive freeze-pump-thaw cycles and then vacuum transferred at room temperature into a clean Pyrex finger, yielding a white solid which gave a clear liquid when melted. The vapor pressure of MITC was measured with a Hg manometer to be 12.8 ± 0.5 torr at T = 297 K. CS_2 was identified as the sole impurity by MS (m/e = 76) and FTIR (1530 cm^{-1}).[24] It was observed to build up slowly, probably via a heterogeneous mechanism, and could be removed by pumping on the MITC sample at T = 195 K ($[CS_2] < 0.5\%$). The MITC sample was kept covered with a black cloth at all times.

CH_3NC (96%) was obtained from Karl Industries, Sapon Laboratories Division (Aurora, OH) and was received as a dark brown liquid. The sample was degassed and vacuum transferred from 279 to 77 K, yielding a clear liquid which turned light brown slowly over time. The 1-cm^{-1} FTIR spectrum matched literature spectra[23] and no impurities were detected (< 1%).

III. Results and Discussion

III.A. Ultraviolet Absorption Spectrum of MITC

We have measured the absorption cross section, σ, of MITC in the UV, Figure 2.2. Special attention was focussed on the long wavelength tail which overlaps the spectrum of solar, or actinic, flux.[25] The MITC absorption band extends out to at least 340 nm, but the wavelength interval from 305 to 330 nm accounts for 86% of the total rate for MITC absorption of the actinic flux in the troposphere. For a photodissociation quantum yield of 1.0, the total absorption rate of 6.7×10^{-6} s^{-1} yields a

lifetime with respect to photolysis of 41 hours, for July 1, noon sunlight at a latitude of 40° N (see Table 2.1). The MITC absorbance was linear in MITC pressure over the range 1.0 - 9.7 torr, as illustrated by the Beer's Law plot in Figure 2.3. The relative uncertainties in the cross sections at the 95% confidence level were 3%, 8%, and 23% at 300, 320, and 330 nm, respectively. With a conservative estimate of ±10% for the systematic error in the cross section determination, the reported values and polynomial fit to the spectrum in Table 2.1 are believed to be correct to within 10% for $\lambda < 300$ nm, 15-20% for $300 \leq \lambda < 320$ nm, and 30% for $320 \leq \lambda \leq 330$ nm. Despite the magnitude of these uncertainties, it is clear that photochemical degradation in the atmosphere could be an effective removal pathway, if the photodissociation quantum yield were sufficiently high. This possibility was explored by quantitatively studying the yield of photolysis products.

III.B. Fundamental Photochemistry of MITC

Neat MITC samples (0.7 - 10 torr) were photolyzed with a 308 nm excimer laser. FTIR spectra revealed that methyl isocyanide, CH_3NC, was the major stable product formed, as shown in Figure 2.4 and Table 2.2. The yield of CH_3NC was then examined with the diode laser flash kinetic spectrometer. Figure 2.5a displays the temporal profile of the CH_3NC produced in the 308-nm photolysis of MITC. The CH_3NC production can be described by the combination of a direct photolytic component and a secondary bimolecular channel, reactions 1 and 2, respectively:

$$CH_3NCS + h\nu\ (308\ nm) \rightarrow CH_3NC + S(^3P) \qquad (1)$$

$$S(^3P) + CH_3NCS \rightarrow CH_3NC + S_2 \qquad (2)$$

From biexponential fits to the CH_3NC rise, it could be estimated that reactions 1 and 2 each contributes approximately 50% of the observed signal. The rate constant k_2 was measured to be $(2.0 \pm 0.3) \times 10^{-11}$ cm^3 $molecule^{-1}$ s^{-1} by fitting a single exponential to the slow component of the CH_3NC rise over the MITC pressure range of 0.092 - 0.32 torr, Figure 2.6. The analogous reaction of $S(^3P)$ with HNCS has been observed and proceeds with a rate constant $\geq 3 \times 10^{-11}$ cm^3 $molecule^{-1}$ s^{-1}.[26]

To determine the photolytic quantum yield for CH_3NC production in reaction 1, 2-methyl-2-butene was introduced to remove the S atoms by forming a thiirane, reaction 3.[27,28]

$$S + CH_3CH{=}C(CH_3)_2 \rightarrow CH_3\overline{CHSC}(CH_3)_2 \qquad (3)$$

Figure 2.7 displays the attenuation of the CH_3NC product signal as a function of the added scavenger. The CH_3NC signal was measured after reactions 1 - 3 were complete and the signal had reached a maximum amplitude. Superimposed on the data is a fit to equation 4, which describes the dependence of the CH_3NC yield on the relative amount of added scavenger.

$$\frac{[CH_3NC]}{[CH_3NCS]^*} = \Phi\left\{1 + \gamma\left(1 + \frac{k_3[2m2b]}{k_2[MITC]}\right)^{-1}\right\} \qquad (4)$$

Equation 4 was derived from a mechanism consiting of reactions 1 - 3; $[CH_3NCS]^*$ represents the initially excited MITC, Φ is the quantum yield for dissociation of excited MITC into $CH_3NC + S(^3P)$ in reaction 1, γ is the yield for CH_3NC production in reaction 2, and 2m2b represents 2-methyl-

2-butene. This analysis is similar to the one employed in determining the CO yield from the reaction of $^1CH_2$ with CH_2CO.[29]

The data in Figure 2.7 suggests that $k_3/k_2 = 0.97 \pm 0.3$ and that $\gamma = 1.12 \pm 0.13$ (the uncertainties are 2σ from the fit). The value of k_3 is expected to lie between the measured rate constants for S-atom reactions with cis-2-butene and 2,3-dimethyl-2-butene at T = 298 K, 6.6×10^{-12} and 4.1×10^{-11} cm^3 $molecule^{-1}$ s^{-1}, respectively.[28] It is predicted to be 1.8×10^{-11} cm^3 $molecule^{-1}$ s^{-1} ($A = 4.7 \times 10^{-12}$ cm^3 $molecule^{-1}$ s^{-1} and $E_a = -0.80$ kcal mol^{-1}), based on an empirical correlation of olefin ionization potentials with their activation energies for reactions with $S(^3P)$.[28] The predicted value of k_3 is consistent with our measured k_2 and the ratio k_3/k_2 extracted from Figure 2.7.

As shown in Figure 2.5b, in the presence of sufficient 2-methyl-2-butene (which prevents S atoms from reacting with MITC in reaction 2) the CH_3NC rise indeed appears to be prompt. The CH_3NC appearance rate in Figure 2.5b is determined by the time constant of the detector (~1 μs), and the signal amplitude is 51% of that in 2.5a. Row 5 of Table 2.2 provides independent evidence which indicates that the yield of CH_3NC as an end-product in the presence of excess scavenger is half of its value in the absence of scavenger, within the experimental uncertainty of ±20%. It thus appears that S atoms quantitatively react with MITC to yield CH_3NC, on the basis of both time-resolved and end-product analyses, and are effectively removed by addition of 2-methyl-2-butene.

Table 2.3 summarizes the results of the time-resolved CH_3NC yield measurements. There was no systematic variation in the results over a broad ratio of 2-methyl-2-butene to MITC pressures, indicating that the scavenging of S atoms was complete to within <5 %. From the CH_3NC

yield, one can calculate the quantity $\sigma(308)\Phi$, the product of $\sigma(308)$, the MITC absorption cross section at 308 nm, and Φ, which is defined above. The yield data indicate that $\sigma(308)\Phi = (8.0 \pm 0.6) \times 10^{-21}$ cm^2, where the uncertainty is the 95% confidence level for precision. Propagating the estimated uncertainties in the measured quantities which factored into the calculation leads to a total relative uncertainty of 17% (2σ). Allowing for the possibility of systematic error in the experimental method, the total system uncertainty is estimated to be 20% and a value of $\sigma(308)\Phi = (8.0 \pm 1.6) \times 10^{-21}$ cm^2 is thus reported. Combining $\sigma(308)\Phi$ with an independent value of $\sigma(308) = (8.1 \pm 1.0) \times 10^{-21}$ cm^2, which was extracted from the Beer's Law plot in Figure 2.3, the value of $\Phi = 0.98 \pm 0.24$ is derived. The measurement of a photodissociation quantum yield near unity is consistent with the lack of structure in the absorption spectrum, which usually suggests a short-lived excited state.[30]

Because our measured quantum yield applies only at the low total pressures employed in these experiments ($P \leq 20$ torr), we carried out the 308-nm photolysis of 0.67 torr MITC in 740 ± 20 torr N_2 and compared it to the equivalent photolysis with no added buffer. Analysis of the resulting FTIR spectra for MITC removal and CH_3NC production (using relative integrated absorptions as summarized in Table 2.2) revealed that Φ at 740 ± 20 torr is equal to the low-pressure value to within the experimental uncertainty of $\pm$ 20%. This suggests that a lower limit for the dissociation rate of excited MITC is 10^{10} s^{-1}, and that our measured values for the MITC UV cross sections and CH_3NC quantum yield can be extrapolated with confidence to atmospheric pressure in order to model the photochemical removal of MITC in the atmosphere.

III.C. Secondary (Photo)chemistry and Environmental Consequences

The photodissociation of MITC into CH_3NC and $S(^3P)$ with a 308-nm photon leaves the products with ~4600 cm^{-1} of excess energy, using the following tabulated thermochemical data: $\Delta H_f(CH_3NCS)$ = 27 kcal mol^{-1},[31] $\Delta H_f(CH_3NC)$ = 41 kcal mol^{-1},[32] $\Delta H_f(S)$ = 66 kcal mol^{-1}.[33] There is insufficient energy for production of $S(^1D)$, which lies 9200 cm^{-1} above the ground state triplet.[27] The persistence, fate, and health consequences of CH_3NC should be examined, since it is the principal stable MITC photodegradation product at solar wavelengths. CH_3NC does not absorb light with $\lambda > 260$ nm ($\sigma < 10^{-21}$ cm^2),[34] and would thus be stable with respect to photolysis in the troposphere. At present, no toxicological data exist for CH_3NC; it has an unpleasant odor and is thought to behave like CO in binding to hemeproteins.[35]

The formation of CH_3NCO (methyl isocyanate) in the photolysis of MITC samples in environmental chambers has been observed.[36] We have taken FTIR spectra of the products formed in the 308-nm photolysis of MITC (0.5 torr) in the presence of O_2 (60 torr) and confirmed the presence of CH_3NCO by its absorption band at 2283 cm^{-1}.[24] After sufficient irradiation, the concentration of CH_3NCO is comparable to that of CH_3NC, as evidenced by analyzing their integrated absorptions. SO_2 (1361 cm^{-1}), some unidentified product(s) with bands at 1700, 1150 and 1050 cm^{-1}, and particulate matter were also formed in this experiment. The latter gave the cell contents after photolysis a cloudy appearance and scattered a HeNe laser beam traversing the cell. In some experiments, CO and CO_2 also appeared as products, but they likely arose from wall reactions since they were not observed when a clean cell was used. A representative product FTIR spectrum is shown in Figure 2.8.

CH_3NCO is classified as a toxic chemical and as an extremely hazardous substance by the EPA;[37] the OSHA 8-hour Permissible Exposure Level is 20 ppb.[38] The chemical was the cause of 2000 deaths as a result of an explosion at a Union Carbide plant in Bhophal, India in 1984. In order to assess the likelihood of CH_3NCO production from MITC in the atmosphere, we set out to determine the mechanism of its formation in our system.

The formation of CH_3NCO in the 308-nm photolysis of 0.86 torr MITC and 14.8 torr O_2 could not be detected with the flash kinetic spectrometer on a 200 μs timescale. Based on the somewhat poor detection sensitivity for the CH_3NCO line probed (a sharp feature near 2283 cm^{-1} superimposed on a broad background absorbance), an upper limit of 13% could be placed on the yield of CH_3NCO on short timescales.

FTIR spectra of a mixture of 0.50 torr CH_3NC and 1.5 torr SO_2 irradiated with 308-nm photons (800 pulses at ~24 mJ cm^{-2}) revealed the production of CH_3NCO, although none was produced in the absence of light. No CH_3NCO was produced in a mixture (not irradiated) of 0.26 torr CH_3NC in 250 torr O_2 (the absence of the CH_3NCO band after 1 hour is estimated to represent ≤ 5% of the CH_3NCO produced in the $CH_3NC/SO_2/h\nu$ experiment above), nor was it produced in significant amounts in the photolysis of a mixture of 0.64 torr MITC and 1.4 torr SO_2. In the latter case, some CH_3NCO would be expected as the CH_3NC formed in the photolysis of MITC accumulated and reacted with SO_2, and this easily accounts for the small amount of CH_3NCO observed.

These results strongly suggest that CH_3NCO is produced by the (photo-oxidative) reaction of CH_3NC with electronically or vibrationally excited SO_2, SO_2^*, as shown in reactions 5 and 6.

$$SO_2 + h\nu \rightarrow SO_2^* \quad (5)$$

$$SO_2^* + CH_3NC \rightarrow CH_3NCO + SO \quad (6)$$

Because CH_3NC does not absorb at 308 nm, SO_2 must be the absorbing species which promotes the reaction. SO_2 has a significant absorption cross section at 308 nm, $\sigma = 2 \times 10^{-19}$ cm^2,[39] but it does not dissociate at wavelengths longer than ~220 nm.[33] The formation of CH_3NCO in a fast bimolecular step was verified with the flash kinetic spectrometer, but only to the extent that CH_3NCO transient absorptions could be detected by flashing mixtures of CH_3NC and SO_2, i.e., no quantum yields or rate constants were measured.

The formation of SO_2 in the MITC/O_2 system can be explained by reactions 7 and 8.[33]

$$S + O_2 \rightarrow SO + O \quad (7)$$

$$SO + O_2 \rightarrow SO_2 + O \quad (8)$$

As a consequence of the hypothesis that CH_3NCO is formed in reaction 6, CH_3NCO should not be produced in this system in the absence of SO_2. This was tested by photolyzing a mixture of 0.49 torr MITC, 60 torr O_2, and 310 torr 2-methyl-2-butene (added in excess to scavenge S atoms and prevent SO and SO_2 formation). The FTIR spectrum of the resulting products revealed that indeed no CH_3NCO was produced in this system. An alternate mechanism for production of CH_3NCO, namely the reaction of vibrationally excited CH_3NC with O_2, is not consistent with the data. To ensure that the absence of CH_3NCO production in the MITC/O_2/2-methyl-2-butene experiment did not simply result from quenching of

excited (hypothetically reactive) CH_3NC molecules by the high pressure of 2-methyl-2-butene, rather than to the absence of SO_2 production, the 2-methyl-2-butene was replaced with 250 torr Ar or SF_6, buffer gases capable of quenching the vibrationally excited CH_3NC. Both CH_3NCO and SO_2 were produced in amounts comparable to those produced in the absence of added buffer, effectively ruling out the alternate mechanism.

The secondary chemistry of the MITC/O_2 system in the presence of ultraviolet photons is quite complicated. The observed formation of CH_3NCO can be rationalized by the build-up of SO_2 which can then react with the primary MITC photoproduct CH_3NC according to reactions 5 and 6. In the troposphere, however, localized concentrations of SO_2 are not likely to be sufficiently high, so that the potential for CH_3NCO formation in the atmosphere by this mechanism does not appear to be significant. The reactions of CH_3NC with O_3, NO_x, or HO_2, atmospheric species which can undergo facile O-atom transfer reactions from the ground state, should be examined as potential sources of CH_3NCO. The conversion of alkyl isocyanides to isocyanates by O_3[40] and NO[41] has been observed to occur in solution.

Finally, experiments should be carried out to determine the importance of additional MITC removal pathways, such as reaction with OH, in order to gain a more complete understanding of its fate in the atmosphere. Little is known about the reaction of isothiocyanates with OH. A crude relative measurement of the rate constant for the reaction of MITC with OH yielded a value of 3×10^{-11} cm^3 $molecule^{-1}$ s^{-1},[42] but the results were neither very compelling nor published in a journal. For the related molecule S-methyl-N,N-dimethyl thiocarbamate, $(CH_3)_2NC(O)SCH_3$, an OH reaction rate constant of 1.3×10^{-11} cm^3

molecule^{-1} s^{-1} has been reported.[43] The lifetime of MITC with respect to reaction with OH in the atmosphere can be crudely estimated to be 28 hours assuming a rate constant of 10^{-11} cm^3 molecule^{-1} s^{-1} and an OH concentration of 10^6 cm^{-3}, a typical value for rural areas.[25] It is thus quite possible that the bimolecular reaction with OH competes with photolysis as an MITC removal pathway. The dominant channel will depend on factors such as geographic location, season, and daily atmospheric and meteorological conditions. Similarly, the reaction of OH with CH_3NC could provide an effective pathway for removal of CH_3NC from the atmosphere.

IV. Conclusion

The photolysis of MITC in sunlight was demonstrated to be an efficient removal pathway in the troposphere. The primary products from the 308-nm photolysis were CH_3NC and $S(^3P)$, produced with a quantum yield of 0.98 ± 0.24. The CH_3NC yield at a total pressure of 740 torr was equal to the value at low pressure, and so we conclude that the UV cross sections and dissociation quantum yield measured here are applicable to atmospheric conditions and should be used to model the fate of MITC in the atmosphere. The reaction of MITC with OH should be explored as a possible additional sink of MITC in the atmosphere. Further studies on the chemistry and toxicology of CH_3NC, along with accurate field measurements of MITC, CH_3NC, and CH_3NCO concentrations are needed to adequately assess the health risks resulting from the widespread agricultural use of metam-sodium.

V. References

1. Nihon Schering K. K. and Shionogi and Co., Ltd., *J. Pesticide Sci.* **15**, 297 (1990).

2. SRI International, *Chemical Economics Handbook*, 1993.

3. J. C. Robinson and W. S. Pease, *California Policy Seminar brief* **5**, July, 1993.

4. M. Leistra and S. J. H. Crum, *Water, Air, and Soil Pollution* **50**, 109 (1990).

5. "National Air Quality and Emissions Trends Report, 1987" (Office of Air Quality Planning and Standards, Monitoring and Reports Branch, United States EPA, 1989)

6. M. J. DiBartolomeis *et al.*, "Evaluation of the Health Risks Associated with the Metam Spill in the Upper Sacramento River" (Office of Environmental Health Hazard Assessment, California EPA, September, 1992).

7. F. van den Berg, *Atmos. Environ.* **27A**, 63 (1993).

8. "Ambient Air Monitoring in Contra Costa County during March 1993 after an Application of Metam-Sodium to a Field" (California Air Resources Board, Monitoring and Laboratory Division, 1993).

9. J. Heicklen, *Atmos. Environ.* **16**, 821 (1982).

10. S.-C. Woo and T. C. Chu, *J. Chin. Chem. Soc.* **5**, 162 (1937).

11. C. N. R. Rao, J. Ramachandran, S. Somasekhara, *Curr. Sci.* **27**, 474 (1958).

12. E. Svatek, R. Zahradnik, A. Kjaer, *Acta. Chem. Scand.* **13**, 442 (1959).

13. P. D'Amario, G. Di Stefano, M. Lenzi, A. Mele, *J. Chem. Soc. Faraday Trans. I* **68**, 940 (1972).

14. I. Tokue, A. Hiraya, K. Shobatake, *Chem. Phys.* **117**, 315 (1987).

15. F. J. Northrup and T. J. Sears, *J. Chem. Phys.* **93**, 2337 (1990).

16. I. Tokue, K. Kobayashi, T. Honda, Y. Ito, *J. Phys. Chem.* **94**, 3485 (1990).

17. R. Holland, D. W. G. Style, R. N. Dixon, D. A. Ramsay, *Nature* **182**, 336 (1958).

18. J. E. Nicholas and C. A. Amodio, *J. Chem. Soc. Faraday Trans. I* **76**, 1669 (1980).

19. F. J. Northrup and T. J. Sears, *J. Chem. Phys.* **93**, 2346 (1990).

20. U. Schmidt, K. Kabitzke, I. Boie, C. Osterroht, *Chem. Ber.* **98**, 3819 (1965).

21. R. Jahn and U. Schmidt, *Monatsh. Chem.* **109**, 161 (1978).

22. P. H. Wine, W. L. Chameides, A. R. Ravishankara, *Geophys. Res. Lett.* **8**, 543 (1981).

23. H. W. Thompson and R. L. Williams, *Trans. Faraday Soc.* **48**, 502 (1952).

24. *Aldrich Library of Infrared Spectra, Vapor Phase*, v. 1.

25. B. J. Finlayson-Pitts and J. N. Pitts, *Atmospheric Chemistry: Fundamentals and Experimental Methods* (Wiley, New York, 1986).

26. C. R. Boxall and J. P. Simons, *J. Photochem.* **1**, 363 (1972/1973)

27. O. P. Strausz, in *Sulfur in Organic and Inorganic Chemistry*, A. Senning, Ed. (Marcel Dekker, New York, 1972), vol. 2, chap. 11.

28. D. D. Davis and R. B. Klemm, *Int. J. Chem. Kinet.* **5**, 841 (1973).

29. E. R. Lovejoy, R. A. Alvarez, C. B. Moore, *Chem. Phys. Lett.* **174**, 151 (1990).

30. J . G. Calvert and J. N. Pitts, *Photochemistry* (Wiley, New York, 1967), p. 584.

31. R. Shaw, in *The Chemistry of Cyanates and their Thio Derivatives*, S. Patai, Ed., (J. Wiley and Sons: New York, 1977), Ch. 6.

32. S. G. Lias *et al.*, *J. Phys. Chem. Ref. Data* **17**, Suppl 1, (1988).

33. W. B. DeMore *et al.*, *Chemical Kinetics and Photochemical Data for Use in Stratospheric Modeling, Evaluation Number 9*, JPL Publication 90-1, 1990.

34. B. K. Dunning, D. H. Shaw, H. O. Pritchard, *J. Phys. Chem.* **75**, 580 (1971).

35. H. M. Walborsky and M. P. Periasamy, in *The Chemistry of Functional Groups, Supplement C*, S. Patai and Z. Rappoport, Eds. (Wiley, New York, 1983), p. 836.

36. G. C. Miller (University of Nevada-Reno), personal communication.

37. California Environmental Protection Agency, Chemical List of Lists, 1991.

38. Sigma/Aldrich Material Safety Data Sheet on CD/ROM, revision 2.14.

39. T. J. McGee and J. Burris Jr, *J. Quant. Spectrosc. and Radiat. Transfer* **37**, 165 (1987).

40. H. Feuer, H. Rubinstein, A. T. Nielsen, *J. Org. Chem.* **23**, 1107 (1958).

41. T. Saegusa, S. Kobayashi, Y. Ito, *Bull. Chem. Soc. Jpn.* **43**, 275 (1970).

42. H. Parlar, BASF Report 87/0498.

43. E. S. C. Kwon, R. Atkinson, J. Arey, *Environ. Sci. Technol.* **26**, 1798 (1992).

Table 2.1. Calculated photolysis rate of MITC[a]

Wavelength interval, nm	Estimated actinic flux,[b] 10^{14} photons cm^{-2} s^{-1}	MITC absorption cross section,[c] 10^{-20} cm^2	Photolysis rate,[d] 10^{-6} s^{-1}
295-300	0.031	1.70	0.05
300-305	0.335	1.23	0.41
305-310	1.25	0.852	1.06
310-315	2.87	0.563	1.62
315-320	4.02	0.348	1.40
320-325	5.08	0.196	1.00
325-330	7.34	0.096	0.70
330-335	7.79	0.040[e]	0.31
335-340	7.72	0.017[e]	0.13

[a] A photodissociation quantum yield of 1.0 is assumed; the total photolysis rate is $(6.7 \pm 1.7) \times 10^{-6}$ s^{-1}.

[b] Noon, July 1 sunlight at 40° N latitude; values from ref 25.

[c] The spectra were fit to a polynomial: $\sigma = 2.029 - 0.1184\lambda' + 0.002346\lambda'^2 - (1.74 \times 10^{-5})\lambda'^3 + (3.57 \times 10^{-8})\lambda'^4$, where $\lambda' = (\lambda - 294)$ over the interval 294 to 330 nm.

[d] Rate = $\Sigma\{J(\lambda)\sigma(\lambda)\Phi(\lambda)\}$, where $J(\lambda)$ is the actinic flux, $\sigma(\lambda)$ is the absorption cross section, and $\Phi(\lambda)$ is the photodissociation quantum yield.

[e] Estimated from an MITC spectrum taken at a pressure of 9.7 torr; the uncertainty in these values is estimated to be ±40%.

Table 2.2. Summary of FTIR analysis of CH_3NC production

P(MITC), torr	$P(N_2)$, torr	P(2m2b),[a] torr	CH_3NC integrated absorbance	$\frac{P(CH_3NC)}{P(MITC)}$	Fluence,[b] 10^{19} photons cm^{-2}	Expected yield[c]
0.67	0	0	0.26	0.13	3.0	0.13
0.66	740 ± 20	0	0.27	0.11	3.0	0.13
0.68	0	0	0.13	0.062	1.8	0.078
0.67	730 ± 20	0	0.15	0.061	1.6	0.070
0.70	0	11 ± 1	0.30	0.14	6.0	0.13

[a] 2m2b ≡ 2-methyl-2-butene

[b] Determined from (measured fluence × number of pulses). The average pulse energy was multiplied by 1.2 and 1.07 to account for window losses and back reflections.

[c] $\frac{P(CH_3NC)}{P(MITC)} = (\text{Fluence} \times \sigma(308) \times \Phi) \ / \ 3.7$, where Φ = 1.0 or 2.0 for experiments with or without 2m2b scavenger, respectively; the factor of 3.7 accounts for dilution of the products into the total cell volume.

Table 2.3. Summary of prompt CH_3NC production measurements

P(MITC), torr	P(2m2b),[a] torr	P(CH_3NC),[b] mtorr	Fluence,[c] 10^{16} photons cm^{-2}	$\sigma(308)\Phi$,[d] 10^{-21} cm^2
0.300	15.9[e]	0.134	5.4	8.3
0.298	5.6[e]	0.0857	4.0	7.2
0.293	14.2	0.142	6.0	8.0
0.244	16.3	0.133	6.0	9.0
0.128	7.0	0.0586	5.9	7.8
0.220	9.2	0.0858	5.2	7.6
0.263	11.4	0.111	5.4	7.8

[a] 2m2b ≡ 2-methyl-2-butene.

[b] Determined from the magnitude of the transient absorbance and the measured peak absorption coefficient of the probed CH_3NC line, which was normalized for collisional broadening. CH_3NC was probed near 2140 and 2158 cm^{-1}.

[c] Measured with a calibrated volume absorbing disc calorimeter with the rear CaF_2 cell window removed, and adding 6.7% for back reflection from the two window surfaces. The index of refraction of CaF_2 at 308 nm is 1.453 (D. F. Bezuidenhout, in *Handbook of Optical Constants of Solids*, E. D. Palik, Ed. (Academic, San Diego, 1991), p. 831). A 7.0-mm diameter circular mask was placed before the cell to define the cross-sectional area of the excimer beam.

[d] $\sigma(308)\Phi$ = P(CH_3NC) / [P(MITC) × fluence].

[e] 3.8 torr of SF_6 was also added as a buffer.

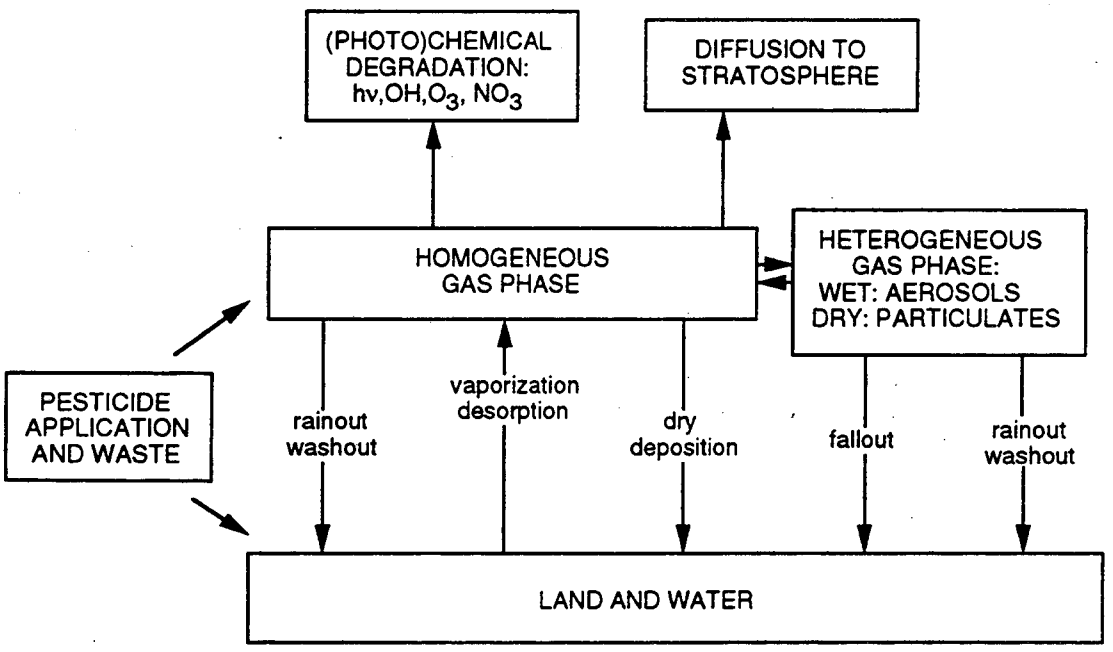

Figure 2.1. Schematic of possible fates of a pesticide in the environment. Pesticides may enter the troposphere by spray drift during application or subsequent volatilization. The partitioning between the different compartments (soil/water/air) and attendant fate are determined by the chemical and physical properties of the pesticide.

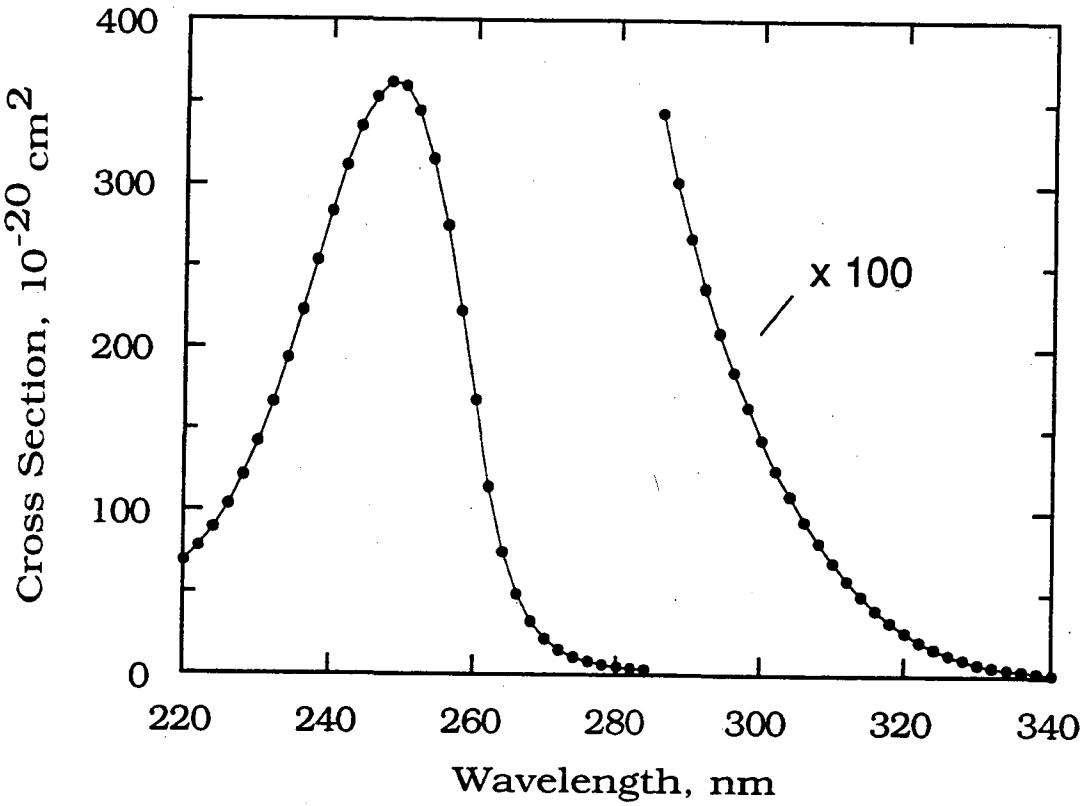

Figure 2.2. Ultraviolet spectrum of CH_3NCS. The CH_3NCS was pumped at 195 K prior to use to remove any CS_2 impurity, as verified by MS and FTIR ($[CS_2] \leq 0.5\%$). An 8.0-cm quartz cell held the sample and the evacuated cell served as the blank for all scans. The 100% transmittance level was determined by averaging the %T values in the 340 to 360 nm range where no signal was detected. All spectra were taken at 298 ± 2 K where σ = Absorbance(base e) / [P(MITC) × (3.25×10^{16}) × 8.0].

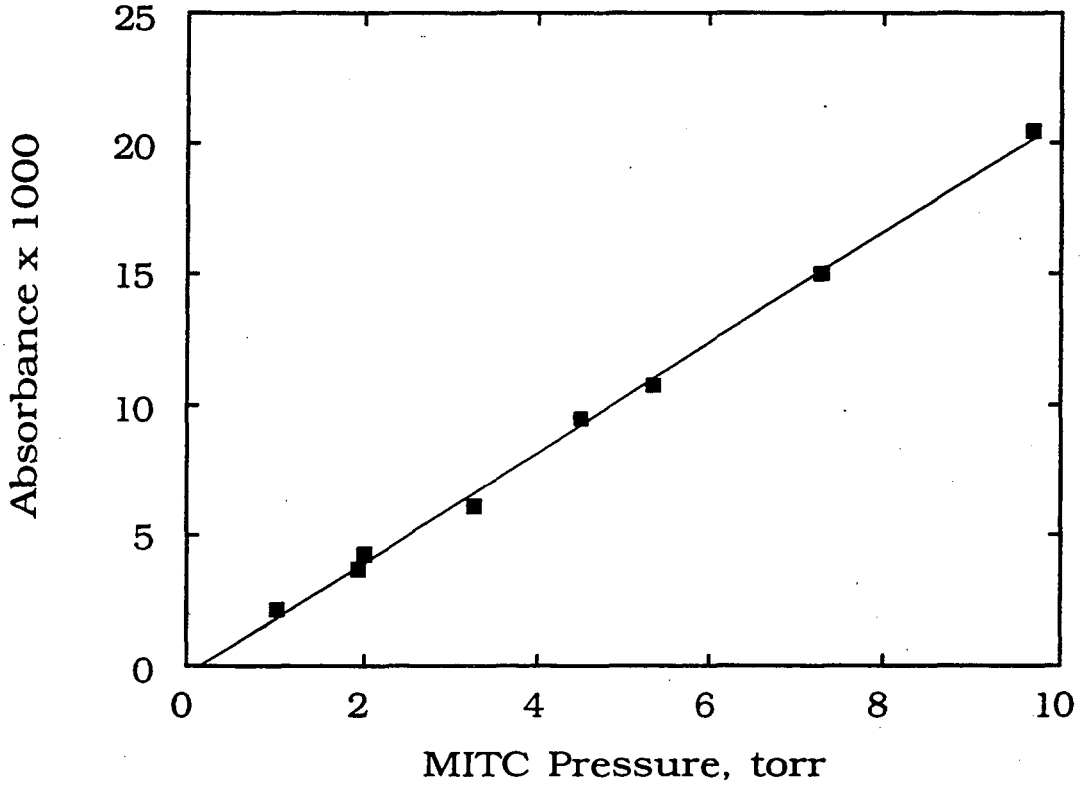

Figure 2.3. Beer's Law plot of the MITC absorbance at 308 nm extracted from the UV spectrum. The slope of the linear least-squares fit indicates that $\sigma(308) = 8.1 \times 10^{-21}$ cm^2.

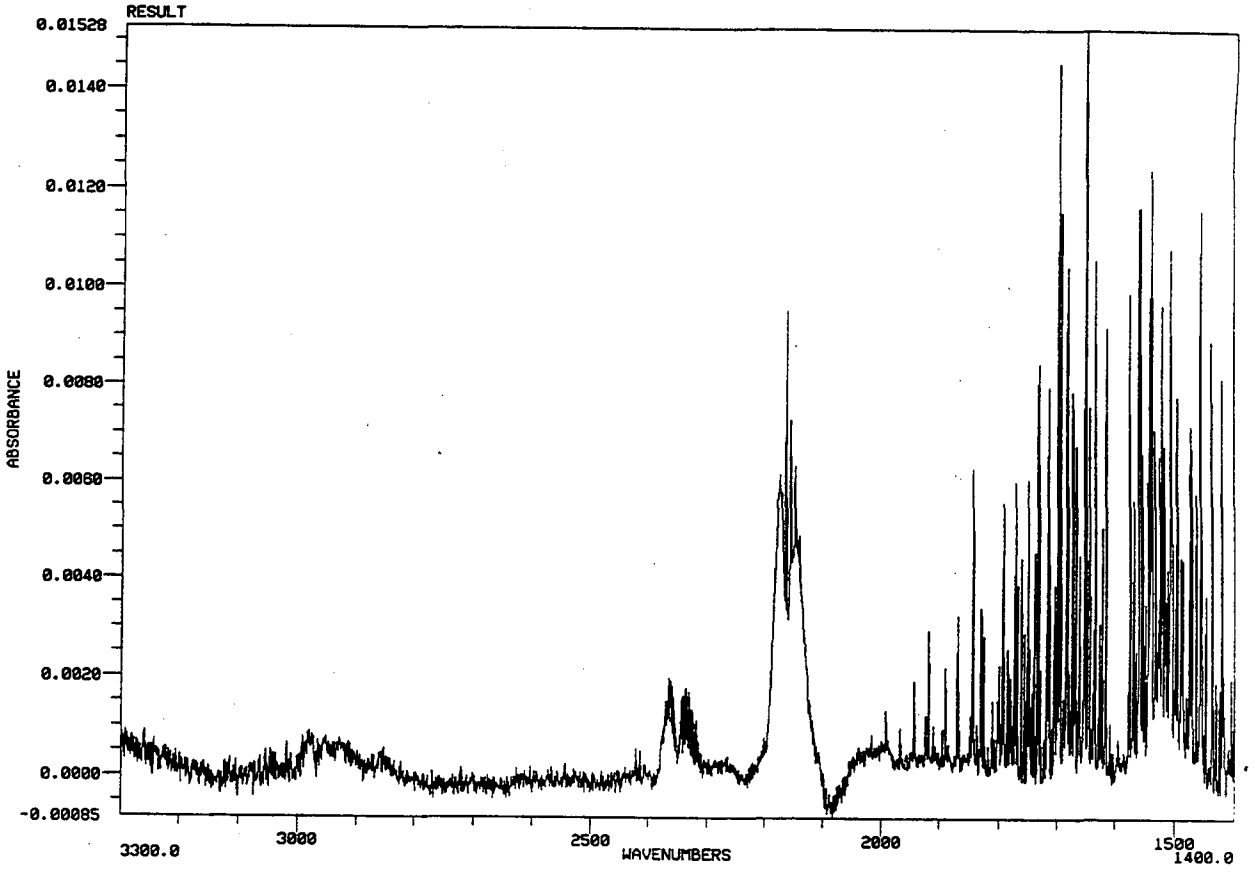

Figure 2.4. FTIR difference spectrum of the products resulting from the 308-nm photolysis (960 pulses, 12 mJ cm^{-2}) of 0.66 torr MITC in 740 torr N_2. All bands are attributed to CH_3NC. The structured absorbance in the 1400 - 2000 cm^{-1} region and the band at 2350 cm^{-1} are due to H_2O and CO_2, respectively, and result from fluctuating background levels. Integration of the 2160 cm^{-1} band (relative to a standard sample) suggests that 73 mtorr of CH_3NC was produced. See Table 2.2 for full analysis.

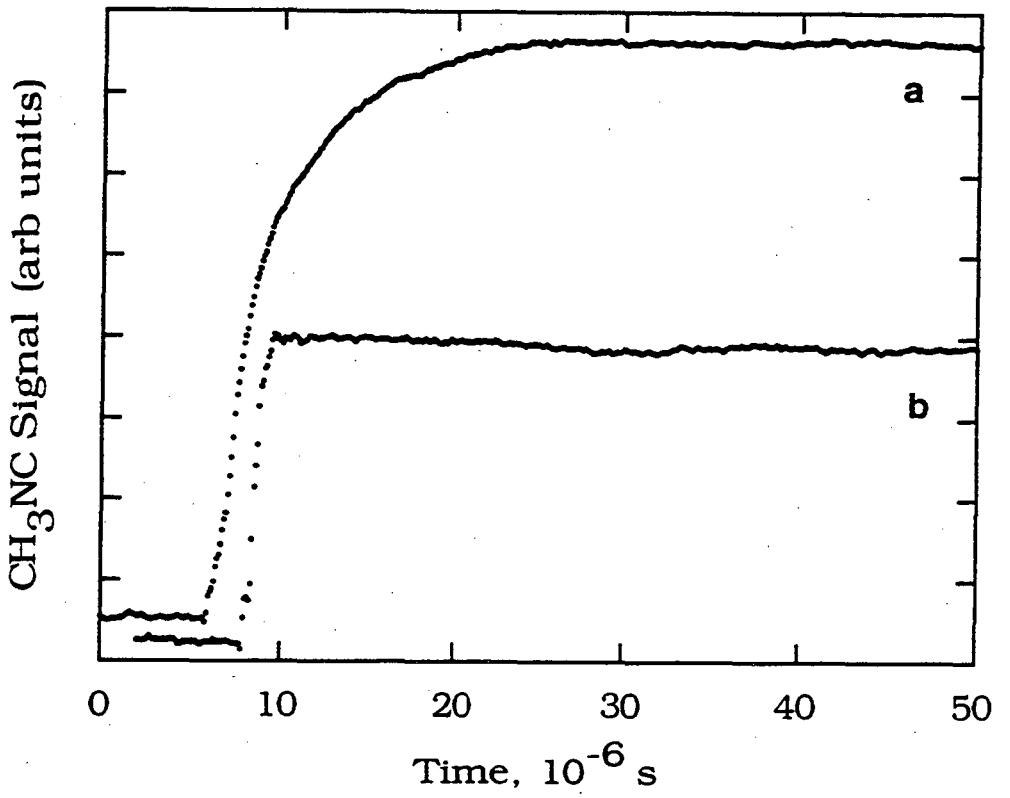

Figure 2.5. CH_3NC temporal profiles from the 308-nm excimer laser photolysis of CH_3NCS obtained with a diode laser flash kinetic spectrometer. Conditions: **(a)** 0.300 torr MITC and 3.8 torr SF_6, **(b)** same as in **a** but introduced 15.9 torr 2-methyl-2-butene into cell. In both traces, the CH_3NC line probed was located at ~2140 cm^{-1} and the UV pulse energy was 32 mJ cm^{-2}. Trace **b** was normalized for the measured collisional broadening by the added 2-methyl-2-butene by multiplying the signal by 2.59. The concentration of CH_3NC in **b** represents 51% of that in **a**, the attenuation resulting from 2-methyl-2-butene scavenging the S atoms produced in reaction 1. Time = 0 was arbitrarily offset for clarity.

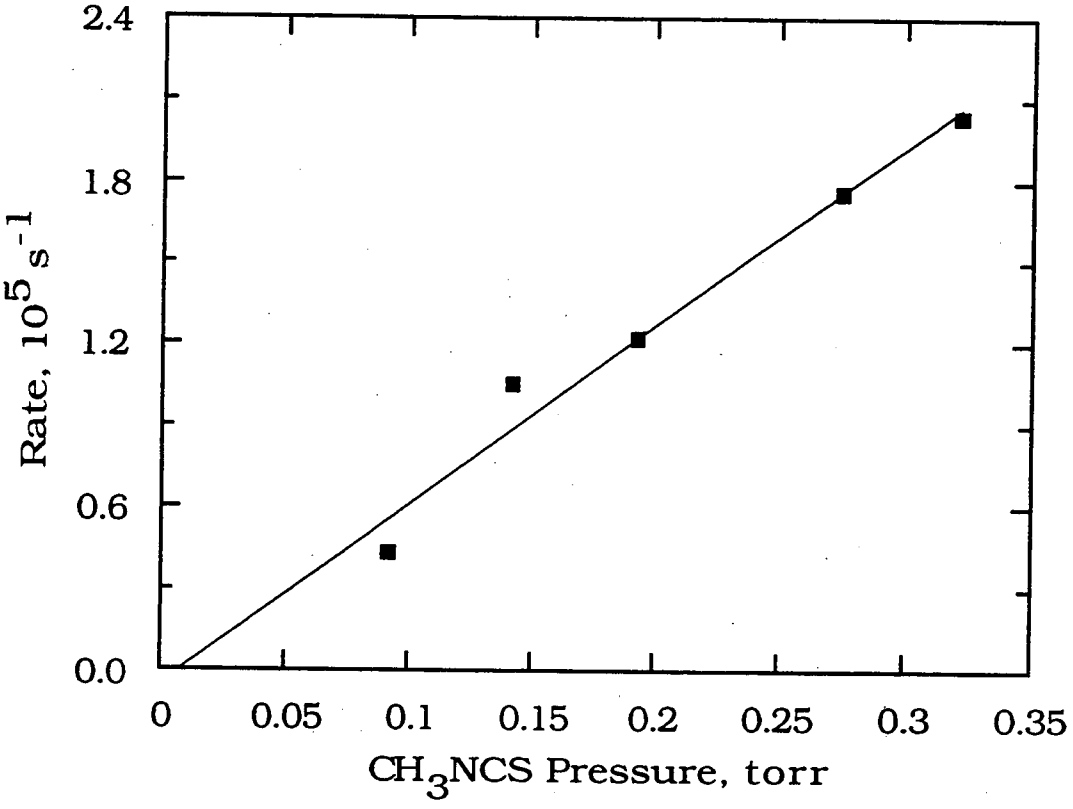

Figure 2.6. Rate constant for production of CH_3NC in reaction 2. The rates were extracted from exponential fits to the slowly rising secondary components of CH_3NC transient signals, such as that shown in Figure 2.5a. The slope suggests that the rate constant $k_2 = (2.0 \pm 0.3)\ 10^{-11}\ cm^3\ molecule^{-1}\ s^{-1}$.

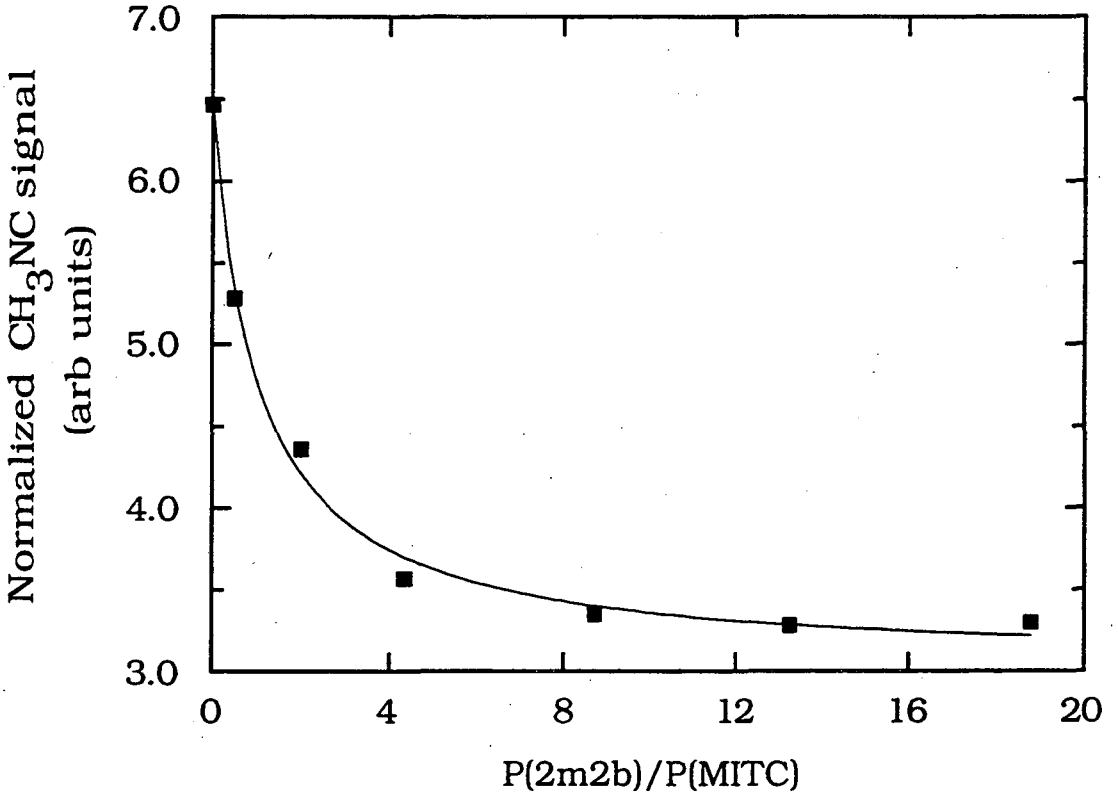

Figure 2.7. Attenuation of the CH_3NC product signal as a function of added 2-methyl-2-butene scavenger. The signals were normalized for collisional broadening due to the added scavenger. The superimposed fit to equation 4 suggests that $k_3/k_2 = 0.97 \pm 0.3$ and that $\gamma = 1.12 \pm 0.13$; the uncertainties are 2σ from the fit.

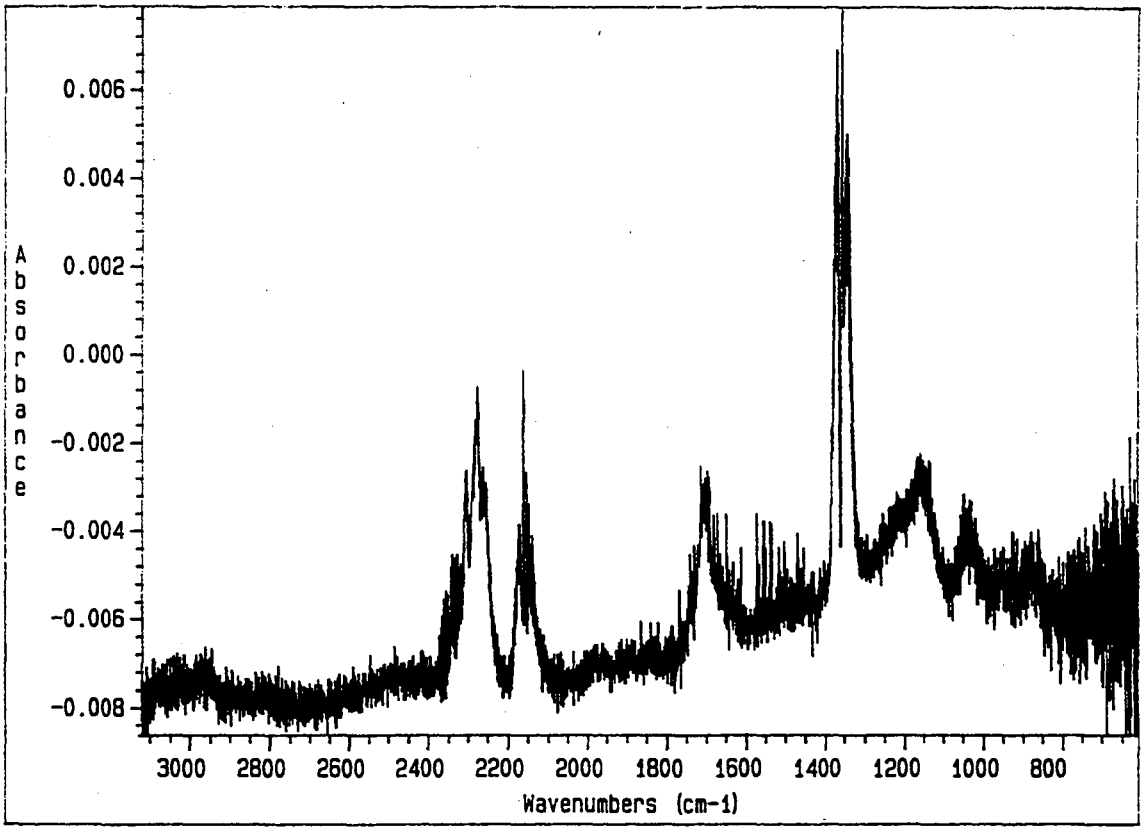

Figure 2.8. FTIR difference spectrum (0.5 cm^{-1} resolution) of the products formed from the photolysis (2000 pulses, 24 mJ cm^{-2}) of a mixture of 0.49 torr MITC, 62 torr O_2, and 250 torr Ar. The major product bands are due to CH_3NC (2166 cm^{-1}), CH_3NCO (2283 cm^{-1}), and SO_2 (1361 cm^{-1}). For this experiment, the cell was carefully washed with acid solution and adapted with new NaCl windows. No CO or CO_2 (above backgound levels) were evident in this spectrum.

Appendix 1. Definition of Beer's Law.[1]

The absorption of incident light, with intensity I_0, by a sample results in a reduction of the transmitted intensity, I. The transmittance, T, is given by $T = (I/I_0)$ and the absorbance, A, is defined as $A = -\ln(T)$. The absorbance of a sample is proportional to the number of absorbing species and the two are related according to Beer's Law. In its most general form, Beer's Law is A = abc, where c is defined as the concentration of the absorbing species, b is the pathlength of the light through the absorbing medium, and a is a proportionality constant related to the ability of a species to absorb a photon. The exact value of a will depend on the units of b and c.

The form of Beer's Law which was employed in Chapter 1 is given by

$$A = -\ln\left(\frac{I_0 - \Delta I}{I_0}\right) = \alpha l P_x \qquad \text{(A1).}$$

In equation A1, ΔI is the transient change in the CW diode laser signal I_0, α is the absorption coefficient at line center ($torr^{-1}\ cm^{-1}$), l is the pathlength (cm), and P_x is the pressure (torr) of the absorbing species at T = 298 K. Equation A1 is used to calculate the pressure of a product species from a measured transient absorption signal.

In addition to using A1 in Chapter 2, another form of Beer's Law was also employed:

$$A = -\ln(T) = \sigma(\lambda) l P_x N_0 \qquad \text{(A2).}$$

In equation A2, $\sigma(\lambda)$ is the absorption cross section (cm^2) at a particular wavelength, l is the pathlength (cm) of the cell holding the sample, P_x is the pressure (torr) of the absorbing species at T = 298 K, and $N_0 = 3.24 \times 10^{16}$ molecules $cm^{-3}\ torr^{-1}$ is a constant which converts the pressure to a number density (molecules cm^{-3}) at T = 298 K, assuming ideal gas

behavior. Equation A2 was used to convert the measured UV spectrum to wavelength-dependent absorption cross sections.

[1] D. A. Skoog, *Principles of Instrumental Analysis* (Saunders: San Francisco, 1985), pp. 160-164.

LAWRENCE BERKELEY LABORATORY
UNIVERSITY OF CALIFORNIA
TECHNICAL INFORMATION DEPARTMENT
BERKELEY, CALIFORNIA 94720

ABH210
LBL Libraries